EXPLORATION GEOPHYSICS
2024, VOL. 55, NO. 6
https://doi.org/10.1080/08123985.2024.2398156

The magnetic gradient tensor of a right circular cylinder: theoretical considerations in the determination of magnetisation direction

K. Blair McKenzie[a,b], Steven M. Hansen[c] and Janet Morrissey[d]

[a]School of Natural Sciences, Macquarie University, North Ryde, Australia; [b]Tensor Research Pty Ltd, Greenwich, Australia; [c]School of Engineering, Macquarie University, North Ryde, Australia; [d]Rio Tinto, Exploration Canada Inc., Thunder Bay, Canada

ABSTRACT

This paper investigates the use of the magnetic gradient tensor and its eigenvectors to derive expressions for estimating the direction of magnetisation of a uniformly magnetised right circular vertical cylinder. Expressions for the gradient tensor, the eigenvalues and eigenvectors, the normalised source strength (NSS), and the direction of magnetisation on the axis of a vertical cylinder are shown to be identical in form to those previously derived for a magnetised sphere or dipole. However, the off-axis gradient tensor field of a vertical cylinder is significantly different to that of a magnetic sphere or dipole particularly at low observation heights. These differences lessen with increasing observation height and in more compact pipes. The normalised source strength displays a directional asymmetry in the eigenvector field of the gradient tensor above a pipe which is related to the direction of magnetisation. This azimuthal asymmetry in the NSS results exclusively from the horizontal components of magnetisation, which are perpendicular to the longitudinal face of the vertical cylinder. In contrast, the vertical component of magnetisation is normal to the circular planar face and produces radial symmetry in the NSS. Additionally, the paper details some unusual properties of the NSS which are attributable to non-dipole field components in the gradient tensor field which cause pairs of eigenvectors to interchange directions when ordered by their eigenvalues, as is done when calculating the NSS. This results in spatial discontinuities in the eigenvector fields arising from crossovers in the ordered eigenvalue surfaces which vary with both magnetisation direction and observation height. This phenomenon is not present in a dipole field and thus provides direct evidence of non-dipole field components. Understanding this complexity in the eigenvector field is essential to designing methodologies which can successfully estimate the direction of magnetisation over a uniformly magnetised cylinder. One proposed method based on the peak NSS, uses airborne gradient tensor data to accurately estimate magnetisation direction over a reversely magnetised pipe-like body in the Diavik diamond field of north-western Canada. The results are verified using a full tensor inversion.

ARTICLE HISTORY
Received 23 August 2023
Accepted 26 August 2024

KEYWORDS
Pipe; magnetic gradient tensor; NSS; magnetisation; eigenvalues; eigenvectors

1. Introduction

The magnetic gradient tensor has emerged as a new technique in geomagnetic exploration which has several important advantages over conventional total magnetic field intensity (TMI) surveys (Pedersen and Rasmussen 1990; Schmidt and Clark 2006; Foss 2006; Clark 2012). In particular, the gradient tensor data are superior to the TMI at low inclinations and in areas of rugged topography. Gradient tensor measurements are less affected by background interference and time varying geomagnetic fields. The magnetic gradient tensor contains more information on magnetic sources than the magnetic field vector and the TMI. Furthermore, the gradient tensor and its eigenvalues and eigenvectors facilitate determination of magnetisation direction and the centre of magnetisation either by inversion or magnetic moment analysis (Phillips et al. 2007; Beiki et al. 2012; Foss and McKenzie 2011; Clark 2012, 2013, 2014; Pratt, McKenzie, and White 2012, 2014; Fullagar and Pears 2015; Foss 2017). This includes estimates of magnetisation direction in regions where there is an anomalous peak in the normalised source strength (NSS) over a variety of compact dipole-like magnetic sources (Beiki et al. 2012; Clark 2012; Pratt, McKenzie and White 2019; McKenzie 2020).

The correct determination of magnetisation direction is extremely important in the interpretation of magnetic field and gradient tensor data (Clark 2012, 2014; Austin et al. 2014; Austin and Foss 2014; Foss 2017; Takahashi and Oliviera 2017). It is essential to the successful modelling and inversion of magnetic targets which may carry remanence, self- demagnetisation and anisotropy of susceptibility. These phenomena can rotate the magnetisation of magnetic bodies away from the

CONTACT K. Blair McKenzie blair.mckenzie@tensor-research.com.au School of Natural Sciences, Macquarie University, North Ryde, NSW 2109, Australia; Tensor Research Pty Ltd, P.O. Box 5189, Greenwich, NSW 2065, Australia

direction of the inducing geomagnetic field (Clark 2014; McKenzie 2020). Incorrect magnetisation directions may lead to erroneous determinations of the position and orientation of magnetic bodies (Austin and Foss 2014).

McKenzie (2022) derived explicit analytical expressions for the magnetic gradient tensor of a uniformly magnetised right circular cylinder. These expressions provide a theoretical basis and methodology for the investigation of magnetisation direction in pipe-like geological bodies including kimberlites (Reed and Witherly 2007), mafic feeder pipes (Pratt, McKenzie, and White 2014) and even holes through basaltic flows. In this paper the terms cylinder and pipe are used interchangeably.

Building on the theoretical results of McKenzie (2022), this paper develops a methodology and conducts a feasibility study into the determination of magnetisation direction of a uniformly magnetised cylinder or pipe from its gradient tensor and from its eigenvalues and eigenvectors. The main objectives of this paper are as follows:

1. To present analytical expressions for the declination and inclination of magnetisation on the axis of a uniformly magnetised right circular cylinder (Section 2). This theory links the normalised source strength (NSS) and other quantities of the gradient tensor field including the eigenvalues, eigenvectors and tensor invariants to the source magnetisation of a vertical pipe.
2. Investigate the off-axis properties of the gradient tensor field of a vertical cylinder using the NSS (Section 3). This includes the documentation of physical properties of the NSS which arise from the source geometry, i.e. cylindrical shape, and its magnetisation direction. How these off-axis properties change with observation height is also investigated. The NSS is an ideal parameter for the delineation pipe-like bodies
3. To demonstrate some both non-dipole and dipole properties of the gradient tensor field of a vertical cylinder and how these change with observation height and axial length (Section 4). This allows classification of the gradient tensor field into near field and far field regions.
4. Section 5 shows that non-dipole behaviour produces discontinuities in the (ordered) eigenvalues and eigenvectors. This behaviour has not been identified or investigated by previous geomagnetic research and is explored in Section 5 using some tools developed for tensor field visualisation by Palacios et al. (2016).
5. In Section 6 we test the feasibility of applying the theoretical results to estimate the direction of magnetisation over pipe-like anomalies using magnetic gradient tensor survey data. The test dataset was collected over a reversely magnetised kimberlite pipe in the Diavik diamond field situated in the Northwest Territories of Canada. The line survey tensor data are used to constrain the physical properties of an anomalous pipe including its location and shape characteristics, magnetisation intensity and magnetisation direction at or in the vicinity of its NSS peak.

2. Theoretical expressions for the determination of magnetisation direction from tensor measurements on the axis of a uniformly magnetised vertical cylinder

2.1. The normalised source strength μ

The normalised source strength (NSS) is a theoretical parameter proposed by Beiki et al. (2012) and Clark (2012) for analysing magnetic gradient tensors. The NSS is a generalisation of the scaled or normalised magnetic moment of a dipole source (Wynn et al. 1975; Wilson 1985; Wynn 1999). The NSS of any magnetic source, denoted by μ, is defined in terms of the eigenvalues of its magnetic gradient tensor, namely,

$$\mu = \sqrt{-\lambda_2^2 - \lambda_1\lambda_3} \quad \text{for} \quad \lambda_1 \geq \lambda_2 \geq \lambda_3, \tag{1}$$

where $\lambda_1 > 0$ is the first or major eigenvalue which is always positive, λ_2 is the second or medium eigenvalue which has the smallest absolute value and $\lambda_3 < 0$ is third or minor eigenvalue which is always negative. Whenever a magnetic field gradient is present, the traceless property of the gradient tensor, together with the ordering of its eigenvalues ensures that the NSS is always real and positive (McKenzie 2020).

The scaled moment vector $\boldsymbol{\mu}$ for a point dipole source of magnetic moment $\mathbf{m}$ is (Wilson 1985; Wynn 1999; Clark, 2012)

$$\boldsymbol{\mu}(\mathbf{r}) = \frac{3C_m\mathbf{m}}{r^4} = \frac{3C_m m}{r^4}\hat{\mathbf{u}}_m = \mu\hat{\mathbf{u}}_m; \mu = \frac{3C_m m}{r^4}, \tag{2}$$

where $\hat{\mathbf{u}}_m$ is the unit vector for the magnetic moment $\mathbf{m}$ and C_m is a constant which depends on the system of electromagnetic used (see Blakely 1995, 67–68). In the SI system of units, $C_m = 100$ nH/m or 100 nTm/A for magnetic fields expressed in nanotesla (nT) and magnetisations expressed in ampere per metre (Am^{-1}). The elements of the magnetic gradient tensor $\mathbf{B}$, its eigenvalues and the NSS are all expressed in nanotesla per metre ($\mathrm{nT\ m}^{-1}$). For a magnetic sphere of radius a and intensity of magnetisation M, the magnitude μ of the scaled moment or NSS at an external point distance r from its centre is

$$\mu(r) = \frac{3C_m m}{r^4} = \frac{4\pi\, C_m M a^3}{r^4}. \tag{3}$$

Clark (2012) and Beiki et al. (2012) showed that the NSS peaks directly over the source for a number of elementary models. In particular, the NSS is independent of magnetisation direction for arbitrary two-dimensional (2D) sources, as well as for spheres and axially magnetised narrow plunging pipes. The NSS peaks directly above the centre of the sphere regardless of the orientation of its magnetic moment, a useful property for locating an unknown source in exploration. This property holds approximately for any compact source with a reasonably coherent magnetisation and possessing a predominantly dipolar external field. Pilkington and Beiki (2013) have stated that the NSS is only weakly dependent on magnetisation direction for a wide variety of 3D magnetic models. We shall review this for the right circular vertical pipe. The Cartesian coordinate system used throughout this paper follows the normal geomagnetic field convention, namely, it is a right-hand clockwise system in which the x axis points north (x-N), the y axis points east (y-E) and the z axis points vertically down (z-D). Hence a magnetisation with a positive inclination $I_M > 0$ and $M_z > 0$ points downwards while a magnetisation with a negative inclination $I_M < 0$ and $M_z < 0$ points upwards. For brevity, these magnetisations are referred to as northern and southern hemisphere magnetisations respectively (regardless of the inclination of the geomagnetic field at their actual location).

Throughout this paper the magnetisation **M** refers to the total magnetisation vector, which is the effective magnetisation resulting from the sum of the induced and remanent magnetisations. We note that the distribution of magnetisation within a magnetised body is heterogeneous over a wide range of scales, and only ellipsoidal and spherical bodies can possess a uniform or homogeneous magnetisation. However in many instances, magnetic sources can be adequately represented by discrete bodies (including a magnetic cylinder) which possess an effectively uniform magnetisation surrounded by a uniformly magnetised or non-magnetic medium (Blakely 1995; Clark 2014). This is provided that the SI susceptibility of the body is considerably less than 1, which ensures that the non-uniform demagnetising field within the source is much less than the applied field so that the resultant field and the corresponding magnetisation are almost uniform.

2.2. Eigenvalues, eigenvectors and the NSS for an axial station: an important special case

The NSS along the axis of a semi-infinite right circular vertical cylinder with magnetisation **M** may be determined analytically by the eigenvalue decomposition of its gradient tensor. An expression for the magnetic gradient tensor on the axis of a semi-infinite a right circular vertical cylinder is given as Equation (46) in McKenzie (2022). This derivation involved substituting special axial forms of the Lipschitz-Hankel integrals defined in McKenzie (2022, Table 3 and Appendix 4) into Equations (37.1)–(37.6) for the six tensor elements B_{xx}, B_{xy}, $B_{xz}, B_{yy}, B_{yz}, B_{zz}$ respectively. In particular from McKenzie (2022, Table 3 and Equations A4.9.7 and A4.9.11), the following integral functions $[I(1,0;0) - (2/r)I(1,1;-1)]$, $[(1/r)I(1,1;0) - (1/2)I(1,0;1)]$, and $I(1,1;1)$ are identically zero on the axis of a right circular cylinder. Hence for a semi-infinite right circular cylinder of radius a and magnetisation $\mathbf{M} = (M_x, M_y, M_z)$, it may be shown that the three diagonal elements are $B_{xx} = -\beta M_z$; $B_{yy} = -\beta M_z$; $B_{zz} = 2\beta M_z$ and the six off-diagonal elements are $B_{xy} = 0 = B_{yx}$; $B_{xz} = -\beta M_x = B_{zx}$;$B_{yz} = -\beta M_y = B_{zy}$ where $\beta = \pi a^2 C_m (a^2 + z^2)^{-3/2}$.

By application of the superposition theorem [McKenzie 2022, Equation (38)], the gradient tensor $\mathbf{B}(0,0,z)$ on the axis of a uniformly magnetised vertical cylinder with radius a and axial length h is.

$$\mathbf{B}(0,0,z) = \begin{bmatrix} B_{xx} & B_{xy} & B_{xz} \\ B_{yx} & B_{yy} & B_{yz} \\ B_{zx} & B_{zy} & B_{zz} \end{bmatrix} = \beta \begin{bmatrix} -M_z & 0 & -M_x \\ 0 & -M_z & -M_y \\ -M_x & -M_y & 2M_z \end{bmatrix}, \tag{4}$$

where

$$\beta = \pi a^2 C_m \left\{ \frac{1}{(a^2+z^2)^{3/2}} - \frac{1}{\left(a^2 + (/z/+h)^2\right)^{3/2}} \right\}.$$

Analytical expressions for the three eigenvalues λ_1, λ_2, λ_3 of the tensor are found by solving for the roots of the characteristic equation $\det(\mathbf{B} - \lambda\mathbf{I}) = 0$ (see Appendix 1). The eigenvalue ordering is determined by the sign of the vertical component of magnetisation M_z. For $M_z > 0$, the ordered eigenvalues $\lambda_1 > \lambda_2 > \lambda_3$ are

$$\lambda_1 = \frac{\beta}{2}\left[M_z + \sqrt{4(M_x^2 + M_y^2) + 9M_z^2}\right] = \frac{\beta}{2}(M_z + \Delta), \tag{5}$$

$$\lambda_2 = -\beta M_z, \tag{6}$$

$$\lambda_3 = \frac{\beta}{2}\left[M_z - \sqrt{4(M_x^2 + M_y^2) + 9M_z^2}\right] = \frac{\beta}{2}(M_z - \Delta), \tag{7}$$

where

$$\Delta = \sqrt{4\,(M_x^2 + M_y^2) + 9M_z^2} = \sqrt{4M_h^2 + 9M_z^2}. \tag{8}$$

The inclination I_M of the magnetisation vector **M** is

$$I_M = \arctan\left[\frac{M_z}{\sqrt{(M_x^2 + M_y^2)}}\right]$$

$$\text{or } I_M = \arctan\left(\frac{M_z}{M_h}\right) \quad \text{for} -\frac{\pi}{2} \le I_M \le \frac{\pi}{2}. \tag{9}$$

As an example, for a vertical magnetisation in the northern hemisphere where $M_z = |\mathbf{M}|$ and $I_M = 90°$, the major eigenvalue λ_1 is largest and the medium λ_2

and minor λ_3 eigenvalues are equal, i.e. $\lambda_1 = 2\beta|\mathbf{M}|$; $\lambda_2 = \lambda_3 = -\beta|\mathbf{M}|$. For this case, the gradient tensor is described as linear degenerate (Palacios et al. 2016). Similarly for a vertical magnetisation in the southern hemisphere where $M_z = -|\mathbf{M}|$ and $I_M = -90°$, the minor eigenvalue λ_3 is greatest in magnitude and the pair of major λ_1 and medium λ_2 eigenvalues are equal (i.e. $\lambda_3 = -2\beta|\mathbf{M}|$; $\lambda_1 = \lambda_2 = \beta|\mathbf{M}|$) so that the gradient tensor on the axis of a right circular vertical pipe is described as planar degenerate.

The normalised source strength $\mu(0,0,z)$ along the axis of a right vertical cylinder is derived from Equations (1) and (5)–(7):

$$\begin{aligned}\mu(0,0,z) &= \sqrt{-\lambda_2^2 - \lambda_1\,\lambda_3}\\ &= \sqrt{-\beta^2 M_z^2 - \left[\frac{\beta}{2}\,(M_z + \Delta)\right]\left[\frac{\beta}{2}\,(M_z - \Delta)\right]}\\ &= \frac{\beta}{2}\,\sqrt{\Delta^2 - 5M_z^2}.\end{aligned}$$

Since the discriminant term is $\Delta = \sqrt{4\,(M_x^2 + M_y^2) + 9M_z^2}$, the final expression for the NSS is

$$\begin{aligned}\mu(0,0,z) &= \frac{\beta}{2}\sqrt{4\,(M_x^2 + M_y^2) + 9M_z^2 - 5M_z^2}\\ &= \beta\sqrt{M_x^2 + M_y^2 + M_z^2} = \beta|\mathbf{M}|\,. \qquad (10)\end{aligned}$$

This result is significant as it shows that the NSS on the axis of a right circular cylinder is independent of the magnetisation direction as is also the case at every point above or around a dipole source or a uniformly magnetised sphere (Clark, 2012; McKenzie 2020).

The magnetisation direction of the source may be determined from the tensor eigenvalues. In the case of a magnetic dipole or a magnetic sphere, the angle between the position vector $\mathbf{r}$ of an observation point (relative to the centre of the source) and the magnetisation vector $\mathbf{M}$ or magnetic moment $\mathbf{m}$ is $\phi = \arccos\left(\frac{\lambda_2}{\mu}\right)$ (Clark, 2012). This angle can also be used for a right circular vertical cylinder with magnetisation $\mathbf{M}$ when the observation point $\mathbf{r} = (0,0,z)$ is at height z on the axis of a vertical cylinder. In this case the ratio $\cos\phi = \lambda_2/\mu$ yields analytical expressions for both the inclination I_M and co-inclination I'_M of magnetisation $\mathbf{M}$. From Equations (6) and (9), this ratio can be written

$$\begin{aligned}\cos\phi &= \frac{\lambda_2}{\mu} = \frac{-\beta M_z}{\beta|\mathbf{M}|} = \frac{-M_z}{\sqrt{M_h^2 + M_z^2}} = \frac{-\mathrm{sgn}\,M_z}{\sqrt{\cot^2 I_M + 1}},\\ &= -\sin I_M \quad \text{for} \quad 0 \le \phi \le \pi \text{ and } -\frac{\pi}{2} \le I_M \le \frac{\pi}{2}. \qquad (11)\end{aligned}$$

The co-inclination angle I'_M is identical to the angle ϕ for a measurement point on the axis of a vertical cylinder. Note that the co-inclination is the angle between the upward pointing vertical axis and the magnetisation vector $\mathbf{M}$ (measured positive clockwise), so that $I'_M = I_M + \frac{\pi}{2}$. Hence I'_M is 180° for a magnetisation at the north magnetic pole, 90° for a magnetisation at the magnetic equator and 0° for a magnetisation at the south magnetic pole. Therefore

$$\begin{aligned}\cos\phi &= \frac{\lambda_2}{\mu} = \frac{-\mathrm{sgn}\,M_z}{\sqrt{\tan^2\,\left(I_M + \frac{\pi}{2}\right) + 1}} = \cos\left(I_M + \frac{\pi}{2}\right)\\ &= \cos I'_M \text{ for } 0 \le I'_M \le \pi\,. \qquad (12)\end{aligned}$$

Thus, for any axial observation point above a uniformly magnetised vertical cylinder, it may be deduced from Equation (12), that the inclination of magnetisation is $I_M = \phi - \pi/2$. This result is identical to that obtained by Clark (2012, Equation 28) for an observation point located directly above a magnetic dipole source, or equivalently, above a magnetic sphere (McKenzie 2020).

The expressions for the rotational and canonical invariants I_1, I_2 and the dimensionless ratio I at an axial observation station may now be expressed in terms of the body magnetisation parameters and the NSS. Combining the expressions for I_1, I_2 and I in Pedersen and Rasmussen (1990) and Clark (2012) (see also Appendix 1) with Equations (5)–(7) for λ_1, λ_2, λ_3 respectively yields:

$$\begin{aligned}I_1(0,0,z) &= \lambda_1\,\lambda_2 + \lambda_1\,\lambda_3 + \lambda_2\,\lambda_3 = -\beta^2(M^2 + 2M_z^2)\\ &= -\beta^2 M^2(1 + 2\cos^2 I'_M\,),\\ &= -\mu^2\,(1 + 2\cos^2 I'_M\,) = -\mu^2\,(1 + 2\sin^2 I_M\,) \qquad (13)\end{aligned}$$

$$\begin{aligned}I_2(0,0,z) &= \lambda_1\lambda_2\lambda_3 = \beta^3 M_z(M^2 + M_z^2)\\ &= \beta^3 M^3 \cos I'_M\,(1 + \cos^2 I'_M),\\ &= -\mu^3 \cos I'_M(1 + \cos^2 I'_M)\\ &= \mu^3 \sin I_M(1 + \sin^2 I_M). \qquad (14)\end{aligned}$$

$$\begin{aligned}I(0,0,z) &= \cos^2\theta = -\frac{27I_2^2}{4I_1^3} = \frac{27\cos^2 I'_M(1 + \cos^2 I'_M)^2}{4(1 + 2\cos^2 I'_M)^3},\\ &= \frac{27\sin^2 I_M(1 + \sin^2 I_M)^2}{4\,\,(1 + 2\sin^2\,I_M)^3}\,. \qquad (15)\end{aligned}$$

These expressions agree with those derived for a magnetic dipole or uniformly magnetised sphere by Clark (2012, Equations (27)–(29)). The expressions in Equations (13) and (14) show that the canonical invariants of Pedersen and Rasmussen (1990) are strongly dependent on the inclination of magnetisation. Furthermore, the dimensionless ratio I is not only determined by the dimensionality of a magnetic source but also by its magnetisation direction. For example, at low magnetic inclinations or when resultant magnetisations are quasi-horizontal, the dimensionless ratio I can be effectively zero over the centres of three-dimensional bodies including vertical pipes, spheres and compact ellipsoids. This is immediately evident

Table 1. Direction of magnetisation parameters for magnetisations in both the north and south magnetic hemispheres as estimated from the eigenvector-eigenvalue decomposition of the magnetic gradient tensor at observation points on the axis of a right circular vertical pipe with uniform magnetisation **M**.

Parameter Name	Northern Hemisphere Magnetisations $I_M \geq 0$ and $M_z \geq 0$	Southern Hemisphere Magnetisations $I_M < 0$ and $M_z < 0$
λ_1	$\lambda_{1N} = \frac{\beta}{2}\ (M_z + \Delta) = -\lambda_{3S}$	$\lambda_{1S} = \frac{\beta}{2}\ (M_z - \Delta)\ = -\lambda_{3N}$
λ_2	$\lambda_{2\mathrm{N}} = -\beta\, M_z(\lambda_{2\mathrm{N}} < 0) = -\lambda_{2S}$	$\lambda_{2S} = -\beta\, M_z(\lambda_{2s} > 0) = -\lambda_{2N}$
λ_3	$\lambda_{3N} = \frac{\beta}{2}\ (M_z - \Delta)\ = -\lambda_{1S}$	$\lambda_{3S} = \frac{\beta}{2}\ (M_z + \Delta)\ = -\lambda_{1N}$
μ	$\mu = \beta\, \lvert\mathbf{M}\rvert$	$\mu = \beta\, \lvert\mathbf{M}\rvert$
ϕ	$\phi = \arccos\left(\frac{\lambda_2}{\mu}\right); \frac{\pi}{2} \leq \phi \leq \pi$	$\phi = \arccos\left(\frac{\lambda_2}{\mu}\right); 0 \leq \phi \leq \frac{\pi}{2}$
I_M	$I_M = \arccos\left(\frac{\lambda_2}{\mu}\right) - \frac{\pi}{2} = \phi - \frac{\pi}{2}$	$I_M = \arccos\left(\frac{\lambda_2}{\mu}\right) - \frac{\pi}{2} = \phi - \frac{\pi}{2}$
I_M	$I_M = \arctan\left(\frac{M_z}{M_h}\right) = \arctan\left(\frac{(B_{zz}/2)}{\sqrt{B_{xz}^2 + B_{yz}^2}}\right)$	$I_M = \arctan\left(\frac{M_z}{M_h}\right) = \arctan\left(\frac{(B_{zz}/2)}{\sqrt{B_{xz}^2 + B_{yz}^2}}\right)$
D_M	$D_M = \arctan\left(\frac{M_y}{M_x}\right) = \arctan\left(\frac{-B_{yz}}{-B_{xz}}\right)$	$D_M = \arctan\left(\frac{M_y}{M_x}\right) = \arctan\left(\frac{-B_{yz}}{-B_{xz}}\right)$
D_M	$D_M = \arctan\left(\frac{\mathrm{e_{jy}}}{\mathrm{e_{jx}}}\right) = D_{evj}; j = 1, 3$	$D_M = \arctan\left(\frac{\mathrm{e_{jy}}}{\mathrm{e_{jx}}}\right) = D_{evj}; j = 1, 3$
D_M	$D_M = \arctan\left(\frac{-\mathrm{e_{2x}}}{\mathrm{e_{2y}}}\right) = D_{ev2} \pm \frac{\pi}{2}$	$D_M = \arctan\left(\frac{-\mathrm{e_{2x}}}{\mathrm{e_{2y}}}\right) = D_{ev2} \pm \frac{\pi}{2}$
I_{ev1}	$I_{ev1N} = \arctan\left[\frac{2\cot I_M}{(3 - \Delta_d)}\right] I_{ev1N} < 0$	$I_{ev1S} = \arctan\left[\frac{2\cot I_M}{(3 + \Delta_d)}\right] = -I_{ev3N}$
I_{ev3}	$I_{ev3N} = \arctan\left[\frac{2\cot I_M}{(3 + \Delta_d)}\right] I_{ev3N} > 0$	$I_{ev3S} = \arctan\left[\frac{2\cot I_M}{(3 - \Delta_d)}\right] = -I_{ev1N}$

Note: It may be shown that $I_{ev3} - I_{ev1} = \pi/2$ for all axial observation points.

from Equation (15) which shows that $I(0,0,z)$ is identically zero above a right vertical cylinder which possesses a zero inclination of magnetisation, i.e. when $I_M = 0°$ or $I'_M = 90°$.

2.3. Expressions for the determination of magnetisation direction

McKenzie (2022) derived expressions for the declination D_M and inclination I_M of magnetisation at an observation height $|z|$ on the axis of a vertical cylinder. These expressions which are shown in Table 1 and Appendix 2 follow from equations for the three magnetic field components b_x, b_y, b_z and from equations for the third column elements B_{xz}, B_{yz}, B_{zz} (or third row elements B_{zx}, B_{zy}, B_{zz}) of the magnetic gradient tensor.

The declination D_M and inclination I_M of magnetisation for a right circular pipe can also be derived from the eigenvector decomposition of the magnetic gradient tensor (McKenzie 2020). Three eigenvectors $\hat{\mathbf{e}}_1, \hat{\mathbf{e}}_2, \hat{\mathbf{e}}_3$ of the magnetic gradient tensor are found by solving the linear equation $\mathbf{B}\,\hat{\mathbf{e}}_\mathrm{j} = \lambda_\mathrm{j}\,\hat{\mathbf{e}}_\mathrm{j}$ for each of the three eigenvalues λ_1,λ_2,λ_3 respectively.

The first eigenvector $\hat{\mathbf{e}}_1 = (e_{1x}, e_{1y}, e_{1z})^T$ at an axial point $\mathbf{r} = (0{,}0{,}z)$ above a vertical cylinder in which $M_z > 0$ and $\lambda_1 = \frac{\beta}{2}\ (M_z + \Delta)$ is

$$\hat{\mathbf{e}}_1 = \frac{\left(1\,, \frac{M_y}{M_x}\,, \frac{2M_h^2}{M_x(3M_z - \Delta)}\right)^T}{\sqrt{1 + \left(\frac{M_y}{M_x}\right)^2 + \frac{4M_h^4}{M_x^2(3M_z - \Delta)^2}}}$$

$$= \frac{\left(1\,, \frac{M_y}{M_x}\,, -\frac{(3M_z + \Delta)}{2M_x}\right)^T}{\sqrt{1 + \left(\frac{M_y}{M_x}\right)^2 + \frac{(3M_z + \Delta)^2}{4M_x^2}}}. \tag{16}$$

The second eigenvector $\hat{\mathbf{e}}_\mathbf{2}$ associated with eigenvalue $\lambda_2 = -\beta\, M_z$ is

$$\hat{\mathbf{e}}_\mathbf{2} = (e_{2x}, e_{2y}, e_{2z})^T = \left(-\frac{M_y}{M_h}, \frac{M_x}{M_h}, 0\right)^T$$
$$= (-\sin D_M, \cos D_M, 0)^T. \tag{17}$$

The third eigenvector $\hat{\mathbf{e}}_3 = (e_{3x}, e_{3y}, e_{3z})^T$ associated with eigenvalue $\lambda_3 = \frac{\beta}{2}\ (M_z - \Delta)$ is

$$\hat{\mathbf{e}}_3 = \frac{\left(1\,, \frac{M_y}{M_x}\,, \frac{2M_h^2}{M_x(3M_z + \Delta)}\right)^T}{\sqrt{1 + \left(\frac{M_y}{M_x}\right)^2 + \frac{4M_h^4}{M_x^2(3M_z + \Delta)^2}}}$$

$$= \frac{\left(1\,, \frac{M_y}{M_x}\,, -\frac{(3M_z - \Delta)}{2M_x}\right)^T}{\sqrt{1 + \left(\frac{M_y}{M_x}\right)^2 + \frac{(3M_z - \Delta)^2}{4M_x^2}}}. \tag{18}$$

By inspection of Equation (16), the declination D_{ev1} and inclination I_{ev1} of the first eigenvector are

$$D_{ev1} = \arctan\left(\frac{\mathrm{e_{1y}}}{\mathrm{e_{1x}}}\right) = \arctan\left(\frac{M_y}{M_x}\right) = D_M$$
$$\text{for } 0 \leq D_M \leq 2\pi\,. \tag{19}$$

$$I_{ev1} = \arctan\left[\frac{\mathrm{e_{1z}}}{\sqrt{\mathrm{e_{1x}^2} + \mathrm{e_{1y}^2}}}\right] = \arctan\left[\frac{2M_h}{(3M_z - \Delta)}\right]$$

$$\text{for } -\frac{\pi}{2} \le I_M \le \frac{\pi}{2}\,. \tag{20}$$

By inspection of Equation (17), the inclination of the second eigenvector is zero and its declination is related to the declination of magnetisation D_M as follows:

$$\tan D_M = \frac{-e_{2x}}{e_{2y}} \text{or } D_M = \arctan\left(\frac{-e_{2x}}{e_{2y}}\right) = D_{ev2} \pm \frac{\pi}{2}. \tag{21}$$

Similarly from Equation (18), the declination D_{ev3} and inclination I_{ev3} of the third eigenvector are

$$D_{ev3} = \arctan\left(\frac{e_{3y}}{e_{3x}}\right) = \arctan\left(\frac{M_y}{M_x}\right) = D_M \quad \text{for } 0 \le D_M \le 2\pi\,. \tag{22}$$

$$I_{ev3} = \arctan\left[\frac{e_{3z}}{\sqrt{e_{3x}^2 + e_{3y}^2}}\right] = \arctan\left[\frac{2M_h}{(3M_z + \Delta)}\right] \quad \text{for } -\frac{\pi}{2} \le I_M \le \frac{\pi}{2} \tag{23}$$

We note that the declination of magnetisation is always calculated using the four-quadrant inverse tangent function, i.e. arctan (y/x) = atan2 (y,x).

The declination of magnetisation on the axis of a vertical cylinder cannot be obtained from the components of the eigenvectors used in Equations (20) and (22) without first constraining D_{ev1} and D_{ev3} to the correct quadrant. This is due to the sign ambiguity of eigenvectors which results in a 180° ambiguity in the determination of the declination in the above equations. To resolve this issue, the inclinations of the first and third eigenvectors I_{ev1} and I_{ev3} are required to be negative and positive respectively for all inclinations on the range $-\frac{\pi}{2} \le I_M \le \frac{\pi}{2}$. Inclinations of the first and third eigenvectors in Equations (20) and (23) may be expressed in terms of the inclination of magnetisation I_M by putting $\cot I_M = \mathrm{M_h}/\mathrm{M_z}$ and defining a dimensionless discriminant term $\Delta_d = \sqrt{4\cot^2 I_M + 9}$. Thus for a magnetisation in the southern hemisphere $-90° \le I_M < 0°$, the inclinations I_{ev1S} and I_{ev3S} (with their ranges shown in parentheses) are:

$$I_{ev1S} = \arctan\left[\frac{2\cot I_M}{(3 + \Delta_d)}\right] \quad \left(0 \text{ to } -\frac{\pi}{4}\right) \text{ and}$$

$$I_{ev3S} = \arctan\left[\frac{2\cot I_M}{(3 - \Delta_d)}\right] \quad \left(\frac{\pi}{2} \text{ to } \frac{\pi}{4}\right).$$

Similarly, for a magnetisation in the northern hemisphere $0° < I_M \le 90°$, the inclinations I_{ev1N} and I_{ev3N} are:

$$I_{ev1N} = \arctan\left[\frac{2\cot I_M}{(3 - \Delta_d)}\right] \left(-\frac{\pi}{4} \text{ to } -\frac{\pi}{2}\right) \text{ and}$$

$$I_{ev3N} = \arctan\left[\frac{2\cot I_M}{(3 + \Delta_d)}\right] \left(\frac{\pi}{4} \text{ to } 0\right).$$

These results are summarised in Table 1. Note that I_{ev1} is negative and I_{ev3} is positive for magnetisations in either hemisphere, and that $I_{ev3} - I_{ev3} = 90°$. For a horizontal magnetisation, $I_{ev1} = -45°$ and $I_{ev3} = 45°$. This sign convention uniquely resolves the eigenvector sign ambiguity and allows for the correct determination of declination from the eigenvector components. Additionally, the expressions for the declination and inclination of the first and third eigenvectors on the axis of a vertical cylinder are in agreement with those for a point dipole and a uniformly magnetised sphere (Clark, 2012; McKenzie 2020, Appendix 5).

3. Investigation of the physical properties of the normalised source strength NSS over a right circular, vertical cylinder both on- and off-axis

This section presents an investigation of the axial- and off-axial properties of the NSS and how these properties change with magnetisation direction, observation height and body shape. A theoretical explanation for the underlying physics of magnetised right vertical cylinders is presented starting with consideration of the magnetic scalar potential which clearly illustrates the interaction between cylindrical shape and magnetisation direction. We show that the symmetry properties of the NSS allow for the spatial delineation of right circular cylindrical bodies and their centres over a range of observation heights.

3.1. A note on the scalar magnetic potential of a vertical cylinder – the effect of magnetisation direction

Expressions for the scalar potential at points coplanar with or above the top face of a semi-infinite vertical cylinder were derived in McKenzie (2022, Equation (13)), namely,

$$\begin{aligned} \mathrm{V}(\mathbf{r}) &= \mathrm{V_a}(\mathbf{r}) + \mathrm{V_r}(\mathbf{r}) \\ &= 2\pi\, a\mathrm{C_m}\{M_r I(1,1;-1) - M_z I(1,0;-1)\}\,, \end{aligned} \tag{24}$$

where $I(1,1;\,-1)$ and $I(1,0;\,-1)$ are Lipschitz-Hankel integrals (Eason, Noble, and Snedden 1955), and $M_r = M_x\cos\theta + M_y\sin\theta$ is the radial component of magnetisation from the axis of the cylinder to the observation point $\mathbf{r} = (r,\theta,z); r = \sqrt{x^2+y^2}$ and $\tan\,\theta = y/x$. This expression shows that the magnetic scalar potential of a vertical cylinder is the superposition of two independent scalar potentials (Siew 1990; Taniguchi 2018). The first is an axial scalar potential $\mathrm{V_a}(\mathbf{r})$ which is radially symmetric and arises from a vertical component of magnetisation M_z. The second is a radial scalar potential $\mathrm{V_r}(\mathbf{r})$ which has azimuthal symmetry and originates from the horizontal (radial) component of magnetisation M_r. Figure 1 shows the axial, radial and total scalar potentials at a standardised observation height $|z|/a = 1$ above a semi-infinite right circular vertical cylinder. The axial scalar potential $\mathrm{V_a}(\mathbf{r})$ displays a maximum over the centre of the cylinder while the radial scalar potential

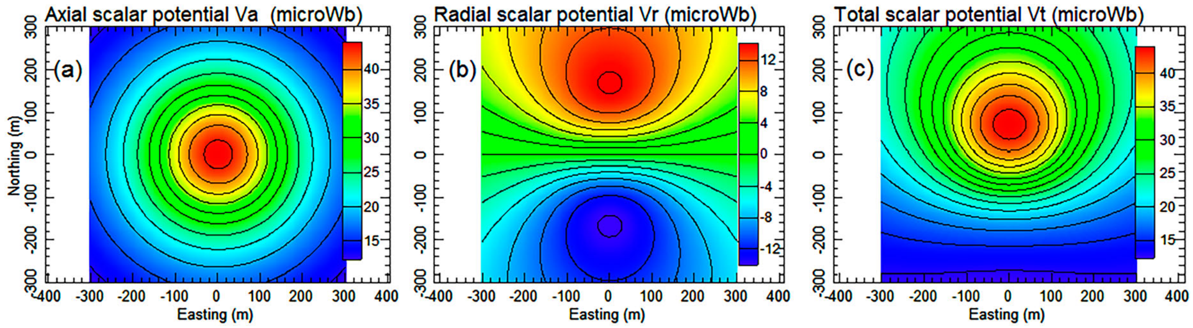

Figure 1. Contoured grid images which show the axial, radial, and total scalar magnetic potentials for a semi-infinite right circular vertical cylinder with radius $a = 100$ m, magnetic moment per unit length $m = 7.50 \times 10^4$ Am, declination $D_M = 0°$ and inclination $I_M = -45°$. The standardised observation height $|z|/a$ is 1.0.

$V_r(\mathbf{r})$ in Figure 1(b) is symmetric and anti-symmetric perpendicular and parallel to D_M respectively. This superposition of potentials causes a shift in the total scalar potential $V_t(\mathbf{r})$ in Figure 1(c) which now peaks off-axis along a direction either parallel or antiparallel to D_M for magnetisations in the southern or northern hemispheres respectively.

3.2. An investigation of the NSS over right circular vertical cylinders

Recently the NSS technique has been successfully applied to the problem of determining the position, magnetic moment and the magnetisation direction of magnetic sources (Beiki et al. 2012; Clark, 2012, 2014; McKenzie 2020). In this section, we investigate the influence of standardised observation height $|z|/a$, the direction of magnetisation and the standardised axial length or shape factor h/a on the properties of the NSS over a series of right circular vertical pipes.

The effect of steepening inclination of magnetisation I_M as the standardised observation height $|z|/a$ increases is illustrated in Figure 2. For magnetisations in the southern hemisphere, i.e. $I_M < 0°$, the NSS images for an observation height $|z|/a = 0.5$ in Figure 2(a, d and g) display a pair of maxima located towards the edges of the cylinder with the larger one, the global maximum $\mu_{\text{pmax}}^{h/a=\infty}$, being located in the direction of magnetisation (parallel to $D_M = 0°$) while the smaller is in the opposite direction (antiparallel to D_M). These positions reverse for magnetisations in the northern hemisphere, i.e. $I_M > 0°$. In contrast with a magnetic dipole or sphere, the NSS displays a local minimum (rather than a global maximum) over the centre of the cylinder, and the uphill horizontal gradient of the NSS no longer points towards the centre of the body. The three images at the low observation height in Figure 2(a, d and g) all display maximum asymmetry parallel to the declination of magnetisation. This asymmetry in the NSS arises purely from the horizontal component of magnetisation M_r, while at higher inclinations, the vertical component of magnetisation M_z dominates rendering the NSS more radially symmetric.

At $|z|/a = 1.0$, the NSS contours in Figure 2(b, e and h) are quasi-elliptical to slightly pear shaped, while for $|z|/a = 2.0$, the NSS is now quasi-circular (see Figure 2(c, f and i)). It is noted that elliptically shaped NSS anomalies, as in Figure 2(b and e), may occur over a right circular vertical pipe and that these anomalies are only related to observation height and the inclination of magnetisation. At observation heights $|z|/a \geq 1$, the NSS images for the low, mid-range and steep inclination models all have a global maximum located over the centre of the circular cylinder. This increasing radial symmetry in the NSS with increasing observation height is directly comparable with that observed in magnetic dipole or magnetic pole sources. We return to this point in Section 4 of the paper.

Figure 3 shows principal profile plots of the NSS parallel and perpendicular to D_M at three standardised observation heights $|z|/a = 0.5$, 1.0 and 2.0 over the centre of the same semi-infinite vertical cylinder displayed in Figure 2(d, e and f) (with $I_M = -45°$). The NSS profiles show significant differences for observation heights above and below $|z|/a = 1$ and also for different directions both parallel to and perpendicular to the declination of magnetisation D_M (shown as solid and dashed lines respectively). For observation heights $|z|/a$ above 1, the NSS profiles in Figure 3(a) display a global maximum over the centre of the semi-infinite vertical pipe model, i.e. the horizontal centre of magnetisation (hcm) is always on the axis of a right circular vertical cylinder for $|z|/a \geq 1$, while for $|z|/a < 1$, the NSS profiles parallel to D_M display a pair of maxima inside the edges of the circular cylinder. Furthermore, the NSS profiles in the direction of magnetisation are asymmetric (except for $I_M = 0°$ and $I_M = \pm 90°$) and double peaked with a global maximum parallel or antiparallel to $D_M = 0°$, while the NSS profiles perpendicular to D_M, are symmetric across the central axis of the vertical cylinder as shown in Figure 3(b). The NSS profiles in Figure 3(b) and the NSS maxima parallel, antiparallel and perpendicular to D_M in Figure 4(a and b) display a degree of complexity which is dependent upon the observation height and the inclination of magnetisation.

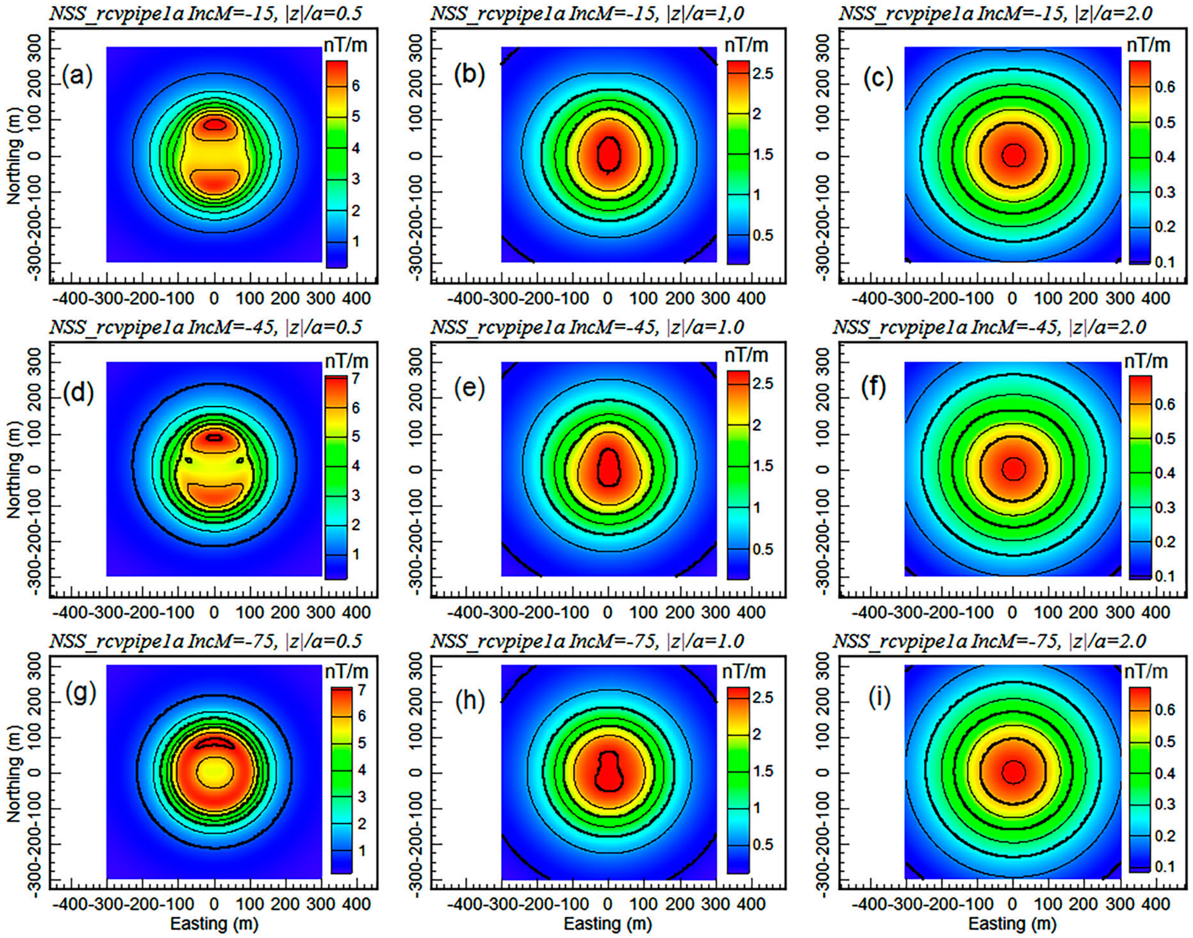

Figure 2. Contoured grid images of the NSS computed over a horizontal plane at three standardised observation heights $|z|/a = 0.5, 1.0$ and 2.0 for a series of semi-infinite, right circular vertical cylinders with radius $a = 100$ m, magnetisation intensity $M = 2.387$ A m^{-1}, declination of magnetisation $D_M = 0°$ and inclination of magnetisation $I_M = -15°, -45°, -75°$. (a–c) show the NSS for a low inclination of magnetisation $I_M = -15°$; (d–f) show images of the NSS for a mid-range inclination $I_M = -45°$, and (g–i) show images of the NSS for a steep inclination of magnetisation $I_M = -75°$.

For example, at low observation heights ($|z|/a \leq 0.3$), the NSS profiles perpendicular to D_M are always double peaked for all inclinations $-90° \leq I_M \leq 90°$ with a pair of equidistant maxima located above opposed edges of the pipe and with a local minimum on the axis of the pipe. At an observation height $|z|/a = 0.5$ in Figure 3(b), the NSS profiles perpendicular to D_M plateau across the central region of the pipe for inclinations below $I_M = -45°$ while at steeper inclinations, the pair of maxima inside the rim of the pipe become more prominent and the local NSS minimum is now located over the centre of the pipe. The NSS maxima decrease in amplitude and migrate inwards towards the centre of the pipe as the standardised observation height $|z|/a$ increases towards one. This symmetry in the NSS profiles perpendicular to D_M is also present in the tensor invariants I_1 and I_2, the dimensionless ratio I, the Frobenius norm $||B||$, and the three eigenvalues $\lambda_i, i = 1, 2, 3$.

In Section 2 we showed that the direction of magnetisation is specified exactly from expressions for the gradient tensor and its eigenvalues-eigenvectors on the axis of a right circular cylinder. These expressions are shown in Table 1. Further to this theory, the investigations in this section have shown that the NSS over a vertical cylinder, whether presenting as an apical peak ($|z|/a \geq 1$) or as a saddle (with an axial minimum) between two opposed peaks ($|z|/a < 1$), always defines the location of the axis quite well. Therefore accurate determinations of magnetisation direction may be obtained on the axis of a right circular cylinder provided that its exact position is known. This proposed methodology is explored in Section 6 using gradient tensor measurements obtained from a helicopter survey over a reversely magnetised pipe in the Diavik diamond field of north-western Canada.

3.3. *The effect of magnetisation direction on the NSS at low observation heights*

Figure 4(a and b) show the change in the maxima of the NSS $\mu_{\max}^{h/a=\infty}$ with increasing inclination of magnetisation I_M (in both hemispheres) for principal profiles parallel, antiparallel and perpendicular to D_M respectively in Pipe Model 1a for $|z|/a = 0.1$ and 0.5.

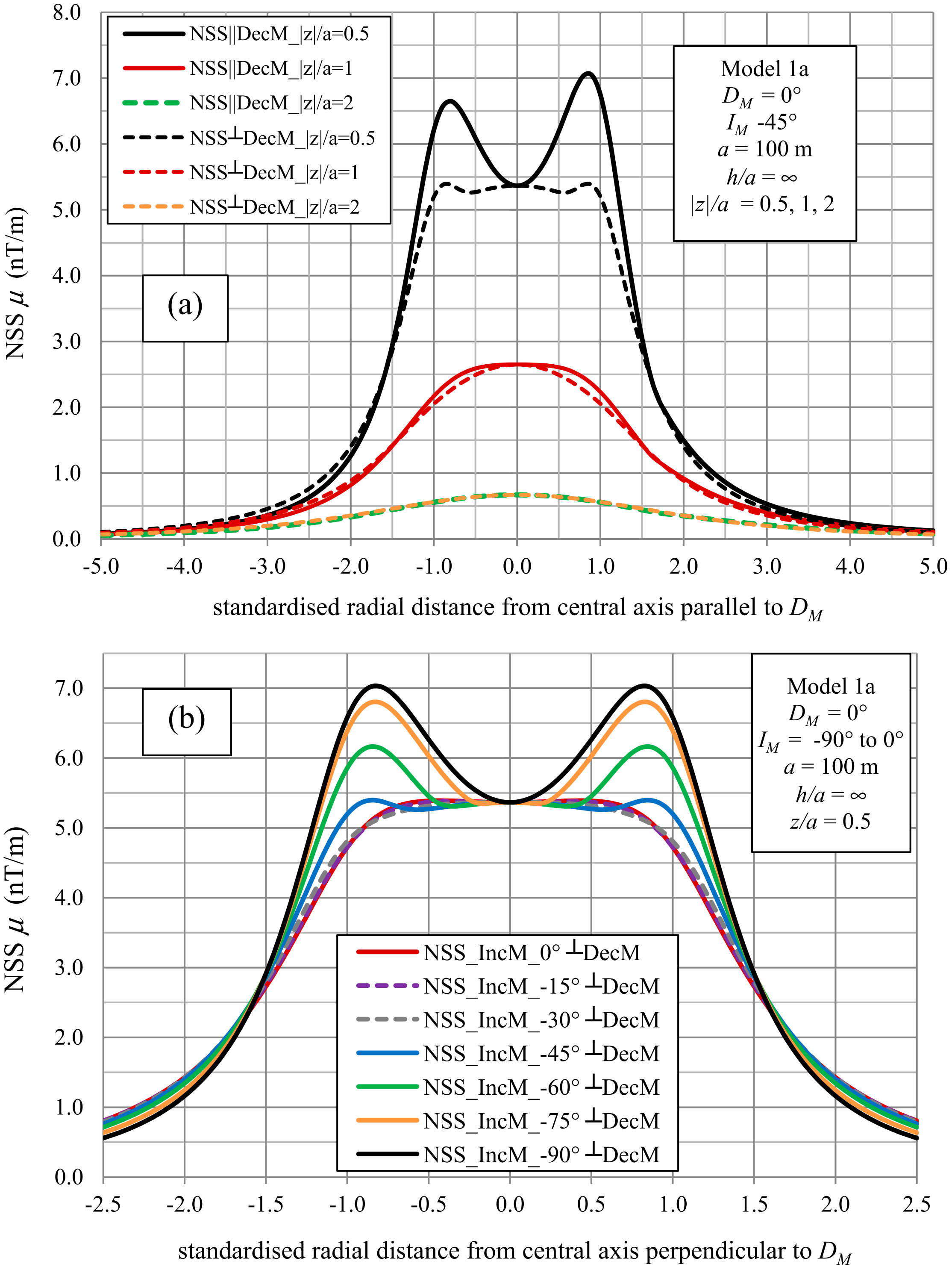

Figure 3. Principal profile plots of the NSS parallel and perpendicular to the declination of magnetisation $D_M = 0°$ over the centre of a semi-infinite right circular cylinder (Model 1a) with magnetisation intensity $M = 2.387\ \text{Am}^{-1}$ and a mid-range inclination of magnetisation $I_M = -45°$. (a) shows the NSS profiles at three standardised observation heights $|z|/a = 0.5, 1.0, 2.0$. (b) shows NSS profiles perpendicular to D_M at $|z|/a = 0.5$ for a range of inclinations I_M from $-90°$to 0°.

Significantly, the NSS global maxima are parallel to D_M for magnetisations in the southern hemisphere ($I_M < 0°$) and antiparallel to D_M for magnetisations in the northern hemisphere ($I_M \geq 0°$).

The parallel D_M and antiparallel $D_M \pm 180°$ plots of the NSS maxima are antisymmetric about $I_M = 0°$ and are mirror images of each other in opposite hemispheres. The maxima in $\mu_{\text{pmax}}^{h/a=\infty}$ are identical for a vertical magnetisation, i.e. $I_M = \pm 90°$, for all three directions. For principal profiles parallel to D_M, the NSS global maxima peak at an inclination in the vicinity of ±60° for both $|z|/a = 0.1$ and 0.5. The NSS secondary maxima antiparallel to D_M have a minimum in the vicinity of $I_M = -30°$ for $|z|/a = 0.1$ and $|z|/a = 0.5$. For profiles perpendicular to D_M, plots of the NSS maxima are symmetric about the zero inclination. In each

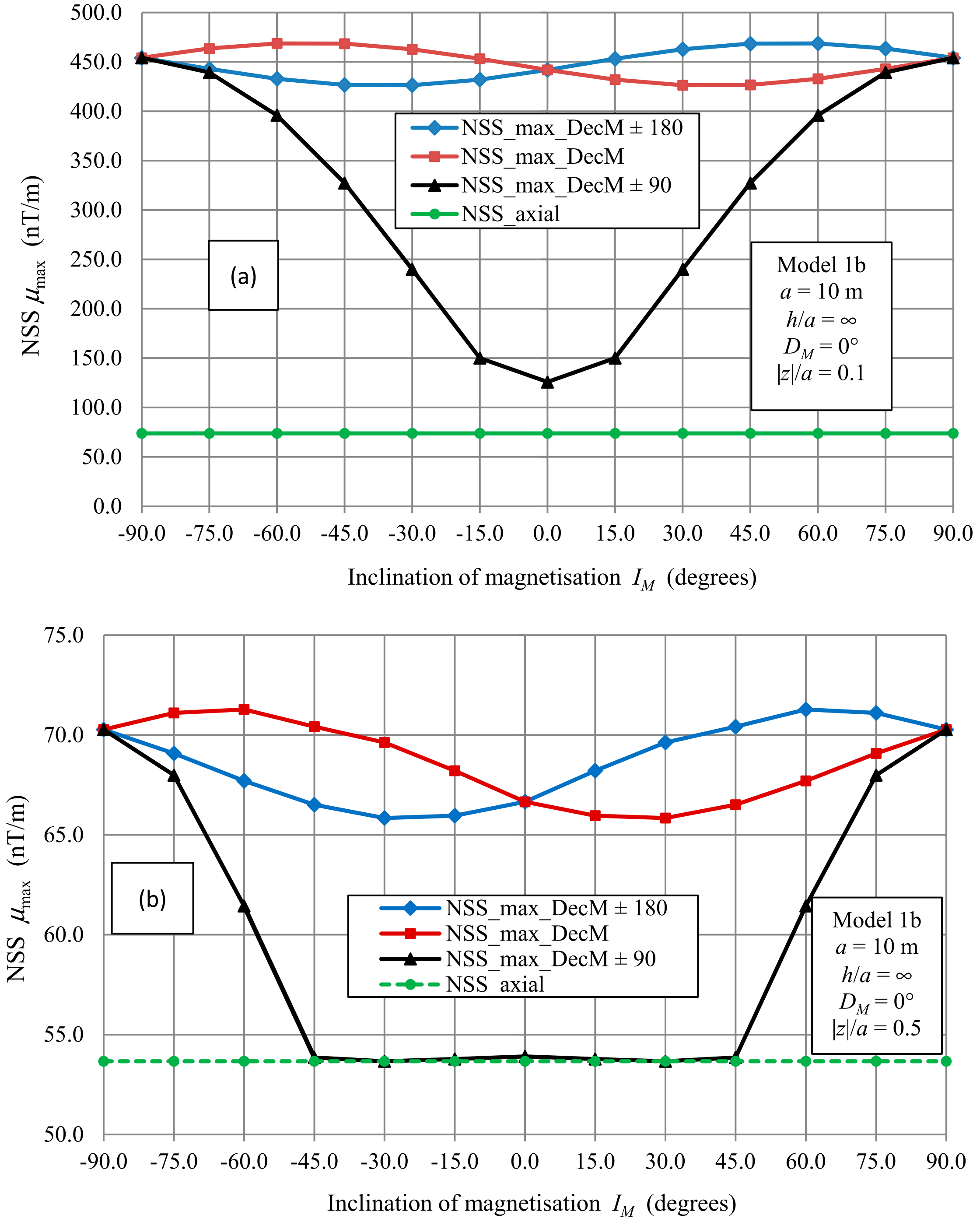

Figure 4. Plots which show the amplitude change in the NSS maxima $\mu_{\text{pmax}}^{h/a=\infty}$, $\mu_{\text{apmax}}^{h/a=\infty}$, $\mu_{\text{ppmax}}^{h/a=\infty}$ with increasing inclination angle I_M (for magnetisations in both the north and south hemispheres) for principal profiles parallel (in red), antiparallel (in blue) and perpendicular (in black) to the declination of magnetisation $D_M = 0°$ respectively in Pipe Model 1b for $|z|/a = 0.1$ (a) and 0.5 (b). The axial NSS is shown in green. The magnetisation intensity is $M = 2.387$ Am^{-1}

hemisphere, the amplitudes of NSS maxima peak at $I_M = \pm 90°$ and then decay rapidly towards lower inclinations. For $|z|/a = 0.1$ the $D_M \pm 90°$ plots have a minimum at zero inclination while for $|z|/a = 0.5$, the maxima decline towards ±45° and then flatten off at mid to low magnetic inclinations, i.e. from $I_M = \pm 45°$ to 0°. It is also significant that the NSS on the axis of the pipe $\mu_{\text{axial}}^{h/a=\infty}$ is no longer equal to the NSS maximum $\mu_{\text{ppmax}}^{h/a=\infty}$ perpendicular to D_M for standardised observation heights $|z|/a$ below 0.5. The overall trend here is that the change in NSS maxima for $D_M \pm 90°$ is far deeper and continues to much lower inclinations as $|z|/a$ decreases towards zero. For example, the ratio of the NSS maxima for $D_M \pm 90°$ at $I_M = 0°$ and $I_M = \pm 90°$ is 27.71% for $|z|/a = 0.1$ and 76.71% for $|z|/a = 0.5$.

At very low sensor heights, i.e. $|z|/a = 0.1$, all three NSS maxima $\mu_{\text{pmax}}^{h/a=\infty}$, $\mu_{\text{apmax}}^{h/a=\infty}$, $\mu_{\text{ppmax}}^{h/a=\infty}$ parallel, antiparallel and perpendicular to D_M are positioned over the rim of the vertical pipe and furthermore, these positions appear to be unaffected by the inclination of magnetisation.

Differences between the axial NSS and NSS maxima perpendicular to the magnetisation direction are negligible for $|z|/a = 0.5$, i.e. 53.5666 nT/m to 53.9053 nT/m (99.37%) but 73.8889 nT/m to 125.8612 nT/m (58.71%) at $|z|/a = 0.1$. This difference implies the presence of significant non-dipole moments at very low observation heights above a vertical pipe. The ratio of the axial NSS to the global NSS maximum represents the relative dipole contribution to the global NSS maxima at each observation height, namely, 75.29% at $|z|/a = 0.5$ and 15.77% at $|z|/a = 0.1$.

3.4. A note on the NSS anomaly half-width

Anomaly half-widths are important indicators of source size and depth in magnetic exploration. These characterise some simple body types such as poles, dipoles, edges, thin dykes which are used in inversion and depth estimation (Clark, 2012). The NSS of a long or compact vertical cylinder peaks over its centre for all observation heights $|z|/a \geq 1$. This enables direct comparisons between the half-widths of the NSS along different directions parallel, antiparallel, and perpendicular to the declination of magnetisation. Appendix 3 presents results showing the effect of magnetisation direction and observation height on NSS half-widths for a series of standardised observation heights ranging from $|z|/a = 1$ to 10 and inclinations of magnetisation ranging from $I_M = -90°$ to 0°. These results are summarised briefly as follows.

The NSS half-widths and half-width to depth ratios $x_{\mathrm{hw}\mu}/|z|$ for vertical cylinders possessing non-vertical magnetisations show strong dependence on the declination and inclination of magnetisation. First the measured NSS half widths vary for principal profiles parallel, antiparallel and perpendicular to the declination of magnetisation. This dependence on magnetisation direction is due to azimuthal asymmetry in the NSS of a vertical cylinder which is not present in point pole or dipole sources (Clark, 2012). Second, the half-width ratios $x_{\mathrm{hw}\mu}/|z|$ for a vertical cylinder are wider than those for both the point pole and dipole (magnetic sphere) sources and that these ratios show a complex dependence on the inclination of magnetisation for observation heights $|z|/a \geq 2$. Third, vertical cylinders with a vertical magnetisation all display NSS half-widths almost identical to that of a point pole for observation heights $|z|/a \geq 6$.

3.5. The effect of axial length on the NSS

The standard axial length of a vertical cylinder ranges from near zero to semi-infinite. Figure 5 shows plots of the NSS for a series of south–north (S-N) and west–east (W-E) principal profiles parallel and perpendicular to the declination of magnetisation D_M for a series of right circular vertical pipes (Model 1a) in which the standardised axial length is varied as $h/a = 0.2, 2, \infty$. The standardised observation height is $|z|/a = 0.5$ and the inclination of magnetisation $I_M = -45°$. These standardised axial lengths correspond to a circular plate or thin disc ($h/a = 0.2$), a compact pipe body in which its diameter is equal to its vertical height ($h/a = 2$), and a semi-infinite pipe ($h/a = \infty$) respectively. The plots in Figure 5 illustrate strong asymmetry in the NSS for directions parallel, antiparallel and perpendicular to D_M at low observation heights. This asymmetry is most pronounced for the thin disc model ($h/a = 0.2$) in Figure 5 which has a local minimum over the axis of the pipe for profiles parallel and perpendicular to D_M. For example, the NSS ratio $\mu_{\max}/\mu_{axis}$ is 2.19, 1.36, 1.31 for $h/a = 0.2$, 2.0, ∞ respectively. An investigation into the effect of increasing standardised axial length h/a on the normalised NSS maxima is presented in Appendix 4 for a series of vertical pipes with $h/a = 0.1, 0.2, 0.3, 1, 2, 3, 5, 10$. Results are presented for standardised observation heights above and below $|z|/a = 1.0$, i.e. for $|z|/a = 0.5$ and for $1 \leq |z|/a \leq 2$. Furthermore, these results allow for the determination of the effective vertical centre of magnetisation for gradient tensor measurements over a vertical pipe. For example, the effective vertical centres for a series of pipes with $h/a = 0.5, 2, 5$ and $|z|/a = 1$, are located in the uppermost 32.8%, 14.0%, and 5.84% of the total length for each pipe. This implies that magnetisation directions obtained over a long or compact vertical pipe are mostly representative of its uppermost region.

4. The near field and far field regions for a right circular vertical pipe: considerations in the determination of magnetisation direction

Isolated "sweet spot" anomalies may be distal or proximal as noted in Foss and Austin (2023). The distal or far field of a magnetised body is defined as the region where the first order dipole term dominates the magnetic field. It is characterised by the intensity of magnetic moment m, the direction of magnetisation and the centre of magnetisation (Foss and Austin 2023). The proximal or near field region occurs closer to a magnetic source where quadrupole and possibly higher order multipole moments make a significant contribution. The coincidence of peak NSS with source location and inclination of magnetisation for $|z|/a > 1$ or midway between opposed NSS maxima for $|z|/a < 1$ (i.e. where the horizontal centre of magnetisation is known) makes the NSS a very useful means for determining where best estimates of magnetisation direction can be made.

This section investigates the off-axis dipole character of the NSS for a vertical cylinder and how this changes with observation height $|z|/a$ and shape factor h/a. We compare the NSS for a vertical cylinder to the NSS for a magnetised sphere and magnetic pole with a view

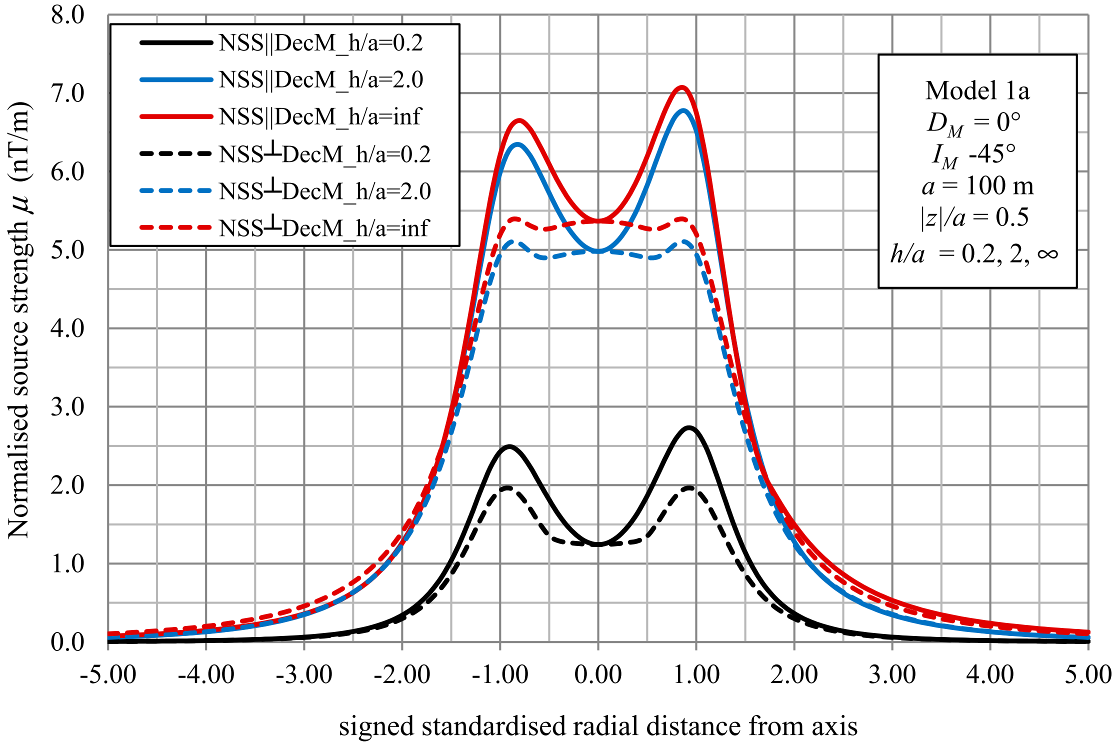

Figure 5. Principal profile plots of the NSS at a standardised observation height $|z|/a = 0.5$ for a series of right circular vertical pipes (Model 1a) in which the axial lengths are $h/a = 0.2, 2.0, \infty$, the magnetisation intensity is $M = 2.387\ \mathrm{Am}^{-1}$, and the inclination of magnetisation $I_M = -45°$.

to defining the near field and far field regions above a vertical pipe. Estimates of magnetisation direction are generally straightforward in the far field or distal region above an isolated compact source which possesses a "sweet spot" magnetic anomaly.

Outside a spherical surface that entirely encloses an arbitrary magnetic source, the magnetic field of that source can be expressed as a infinite series of multipole components known as the Laplace expansion (Cowan 1968; Jackson 1999), i.e. as an infinite sum of multipole contributions with the main dipole term having a falloff of $1/r^3$; a quadrupole term with a falloff of $1/r^4$; an octupole term with a falloff of $1/r^5$ and so on. The quadrupole term is equivalent to a pair of adjacent, oppositely directed dipoles while the octupole term is equivalent to a pair of adjacent, oppositely directed quadrupoles (Clark 2014). How this manifests itself in relation to the direction of magnetisation within a right circular cylinder is unclear, but at low observation heights the multipole moments appear stronger parallel to the declination of magnetisation. The far field is always dominated by the dipole term provided that the dipole moment is non-vanishing. For finite uniformly magnetised bodies of orthorhombic or higher symmetry, for example, ellipsoids, rectangular prisms, right circular or elliptic cylinders, the quadrupole moment is zero and the lowest non-dipole term is usually the octupole contribution (Medeiros and Silva 1995; Clark 2014). For highly symmetric sources including a cube, an octahedron or a right circular cylinder with height/diameter ratio $h/2a \approx 0.9$ (Collinson 1983), the octupole term also vanishes and the source is well represented by a point dipole at relatively short ranges. Medeiros and Silva (1995) state that the quadrupole term in compact 3D bodies is unimportant provided that the observation height above its horizontal centre of magnetisation is greater than the diameter of a sphere enclosing it. This criterion would appear to hold for observation heights $|z| \geq 2a$ above a compact pipe where $h/a \leq 2$.

To investigate the influence of elevation at which the magnetic gradient tensor is measured, the ratios of the NSS have been calculated for a magnetic sphere with radius a and a series of right circular vertical cylinders with $h/a = 4/3$, 2, and ∞. For purposes of comparison, the cylinder with standardised axial length $h/a = 4/3$ has the same moment $\mathbf{m} = \frac{4}{3}\pi\, a^3\, \mathbf{M}$ as an equivalent magnetic sphere with radius a and magnetisation $\mathbf{M}$. From Equations (1) and (2), the NSS for a magnetic sphere with radius a and intensity of magnetisation M is $\mu_s(0{,}0{,}z_s) = \frac{3\mathrm{C_m} m}{z_s^4} = \frac{4\pi\, \mathrm{C_m} a^3 M}{z_s^4}$, and for the right circular vertical cylinder of axial length h, the NSS on its axis at an observation height $|z|$ is

$$\mu_c(0{,}0{,}z_s) = \pi\, a^2\, \mathrm{C_m}\, M \times \left\{ \frac{1}{(a^2+z^2)^{3/2}} - \frac{1}{(a^2+(|z|+h)^2)^{3/2}} \right\}. \tag{25}$$

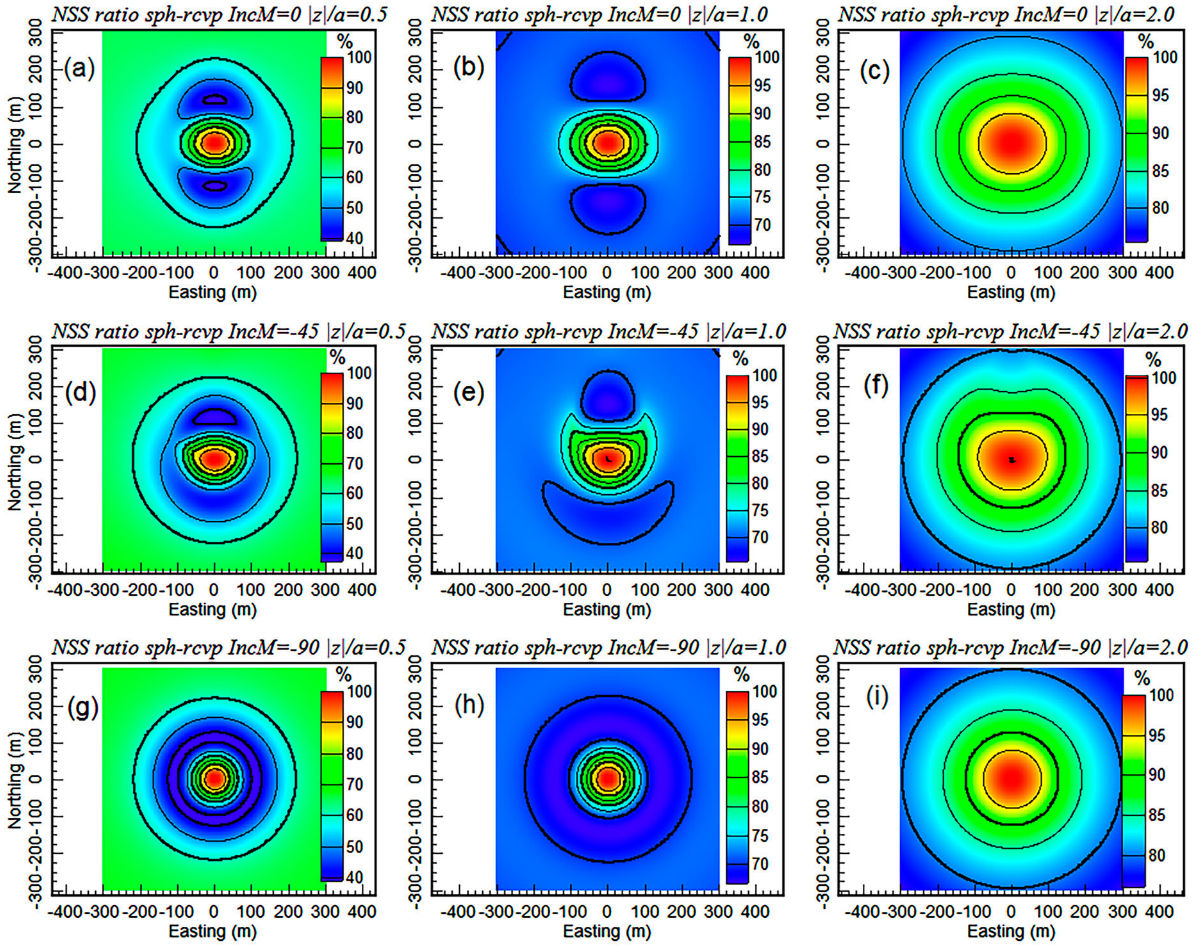

Figure 6. Contoured grid images of the NSS ratios (in per cent) for a magnetic sphere and a compact right circular vertical cylinder ($h/a = 2$) computed over a horizontal plane at three standardised observation heights $|z|/a = 0.5$, 1.0 and 2.0 for a series of semi-infinite, right circular vertical pipes with radius $a = 100$ m, declination of magnetisation $D_M = 0°$ and inclination of magnetisation $I_M = 0°, -45°, -90°$. (a–c) show images of the NSS ratios for $I_M = 0°$; (d–f) show images of the NSS ratios for $I_M = -45°$; and (g–i) show images of the NSS ratios $I_M = -90°$.

Therefore the observation height z_s at which μ_s and μ_c are equal is

$$z_s = \sqrt{2}a\left\{\frac{1}{[1+(z/a)^2]^{3/2}} - \frac{1}{[1+(|z|/a+h/a)^2]^{3/2}}\right\}^{-1/4} \qquad (26)$$

For a magnetic point pole which is represented by a long narrow vertically magnetised circular pipe (Clark, 2012), the normalised source at a point $\mathbf{r} = (0,0,z_p)$ on its axis is $\mu_p = \frac{C_m \pi a^2 |M_z|}{z_p^3}$. Then for a vertically magnetised semi-infinite vertical cylinder, the observation heights z_p and z_c at which μ_p and μ_c are equal is $z_p = a\sqrt{1+(z_c/a)^2}$.

Figure 6 shows grid images of the ratios z_s / $|z|$ of the NSS of a dipole (magnetic sphere) and a compact right circular vertical pipe with radius $a = 100$ m and axial length $h = 2a$ as both the standardised observation height and inclination of magnetisation are increased.

For the standardised observation heights $|z|/a = 0.5$, 1.0, 2.0 in Figure 6, the observation heights z_s above the centre of the equivalent magnetic sphere for a compact vertical pipe with $h/a = 2$ are 156.64 , 187.75, and 270.08 m respectively. The ratios z_s / $|z|$ for a series of right circular vertical cylinders and equivalent magnetic spheres which have the same axial NSS are presented in Table A4.1 of Appendix 4. The images in Figure 6 show that regions where the NSS ratios exceed 90% expand greatly in area as the standardised observation height increases. Figure 7 compares the NSS for a vertically magnetised semi-infinite cylinder or pipe to the NSS for a vertically magnetised sphere and magnetic pole. These plots show that for principal profiles perpendicular to D_M at an observation height $|z|/a = 2$, the NSS ratios for the dipole-pipe μ_s/μ_c and pole-pipe μ_p/μ_c both exceed 91 per cent over the full horizontal extent ($2a$) of each magnetic source.

Table 2 shows the average NSS ratios μ_s/μ_c calculated over an area $A = \pi a^2$ directly above the top surface of a series of right circular vertical pipes with $h/a = 4/3$, 2, ∞. The standardised observation heights are $|z|/a = 1$, 2, 3, 4. These NSS ratios exceed 95% in all compact models at observation heights

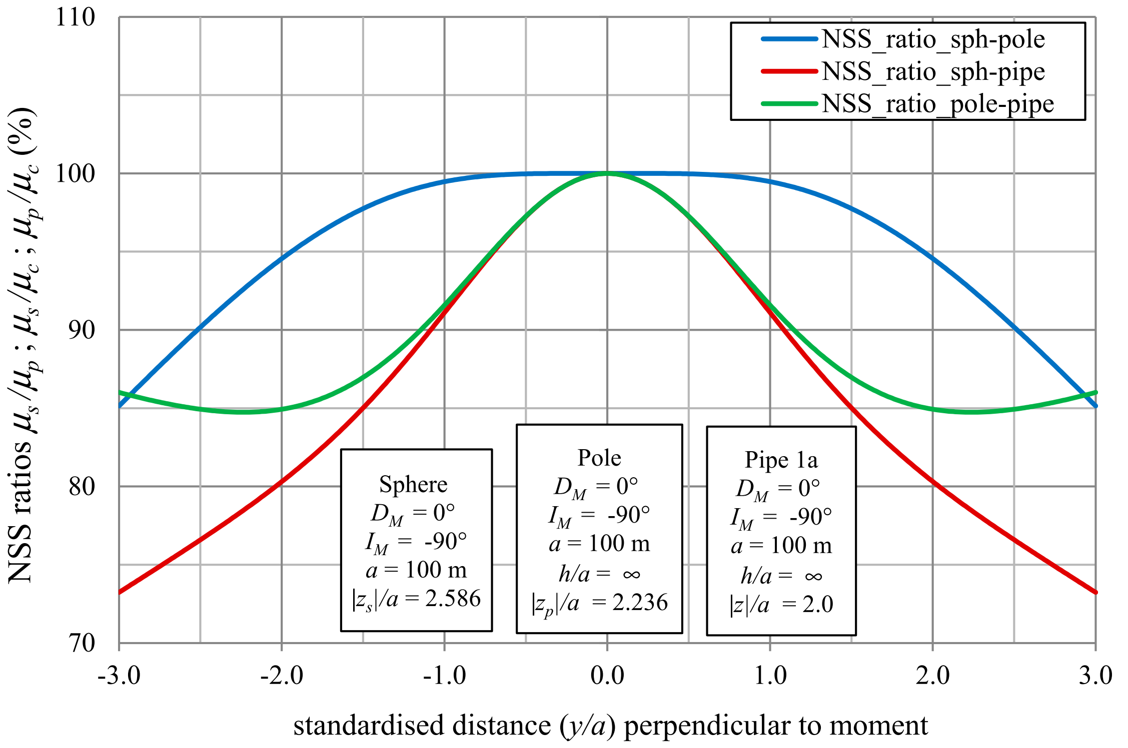

Figure 7. Principal profile plots which compare the NSS for a vertically magnetised semi-infinite vertical pipe to the NSS for a vertically magnetised equivalent magnetic sphere and magnetic pole. The pipe, sphere and pole all have a radius $a = 100\,\mathrm{m}$. The standardised observation height for the vertical pipe is $|z|/a = 2$ which is equivalent to 2.586 for the magnetic sphere and 2.236 for the magnetic pole.

Table 2. The average NSS ratios $\alpha = \mu_s/\mu_p$ (in per cent) calculated over an area $A = \pi\, a^2$ directly above the top surface of a series of right circular vertical cylinders with $h/a = 4/3$, 2, ∞ in which the standardised observation heights are $|z|/a = 1$, 2, 3, 4.

h/a	μ_s/μ_c $\lvert z\rvert/a = 1$	μ_s/μ_c $\lvert z\rvert/a = 2$	μ_s/μ_c $\lvert z\rvert/a = 3$	μ_s/μ_c $\lvert z\rvert/a = 4$
4/3	86.449	97.668	99.401	99.790
2	85.552	96.494	98.485	99.106
∞	84.696	94.881	96.868	97.634

Note: The magnetisation direction is $D_M = 0°$, $I_M = -45°$.

$|z|/a \geq 2$ and exceed 99% at $|z|/a \geq 4$. We note further that the μ_s/μ_c ratios decrease slightly as the vertical pipes become more elongated, but more significantly, the μ_s/μ_c ratios increase with increasing observation height over the range $1 \leq |z|/a \leq 2$.

The effect of increasing axial length h/a of vertical pipes is further illustrated in Figure 8 which shows the NSS ratios parallel to the magnetisation direction ($D_M = 0°$, $I_M = -45°$) at a standardised observation height $|z|/a = 4$ for a series of right circular vertical pipes with $h/a = 4/3, 2, \infty$. The dipole contribution to the NSS exceeds 90% over the central region of the pipe but this changes significantly in the semi-infinite pipe as the radial distance increases (see Figure 8). For example at a standardised radial distance $x/a = 3$ parallel to the moment $D_M = 0°$, the dipole contributions to the NSS are 97.57%, 89.19% and 72.55% for $h/a = 4/3, 2, \infty$ respectively.

Another parameter which reflects the dominance of the dipole term is the effective area or areal coverage S_α of regions where the NSS ratios exceed a predetermined level α. For a vertical pipe with radius a, the standardised coverage parameter S_α may be estimated as.

$$S_\alpha = (1/a)\sqrt{d_{||}^{\alpha}\, d_{\perp}^{\alpha}}. \tag{27}$$

where $d_{||}^{\alpha}$ and $d_{\perp}^{\alpha}$ are the radial distances from the central axis of the pipe to points where the NSS ratios exceed a specified level $\alpha = 95\%$ both parallel and perpendicular to the magnetisation direction. Tables of the radial distances $d_{||}^{\alpha}$ and $d_{\perp}^{\alpha}$ parallel and perpendicular to the magnetisation direction at points where the NSS ratios $\alpha = \mu_s/\mu_c$ are 95% are given in Table A5.2 of Appendix 5. This data is used to estimate the standardised areal coverage S_α which is shown in Table 3. The results in Table 3 indicate that S_α is extremely low (< 0.4) for all pipe models at $|z|/a = 1$. This coverage increases to well above 1 for both compact models at $|z|/a = 3$ and at $|z|/a = 4$ for the semi-infinite pipe. Therefore it may be concluded that for sources which are more equidimensional, the dipole approximation is acceptable at shorter ranges than for an elongated source. This is because the relative influence of the longitudinal face lessens while the relative influence of the top face which has radial symmetry (cf. with a dipole) increases as the axial length h/a shortens.

In summary, the NSS ratios shown in Tables 2 and 3 and Figures 6–8 show that the dipole contributions

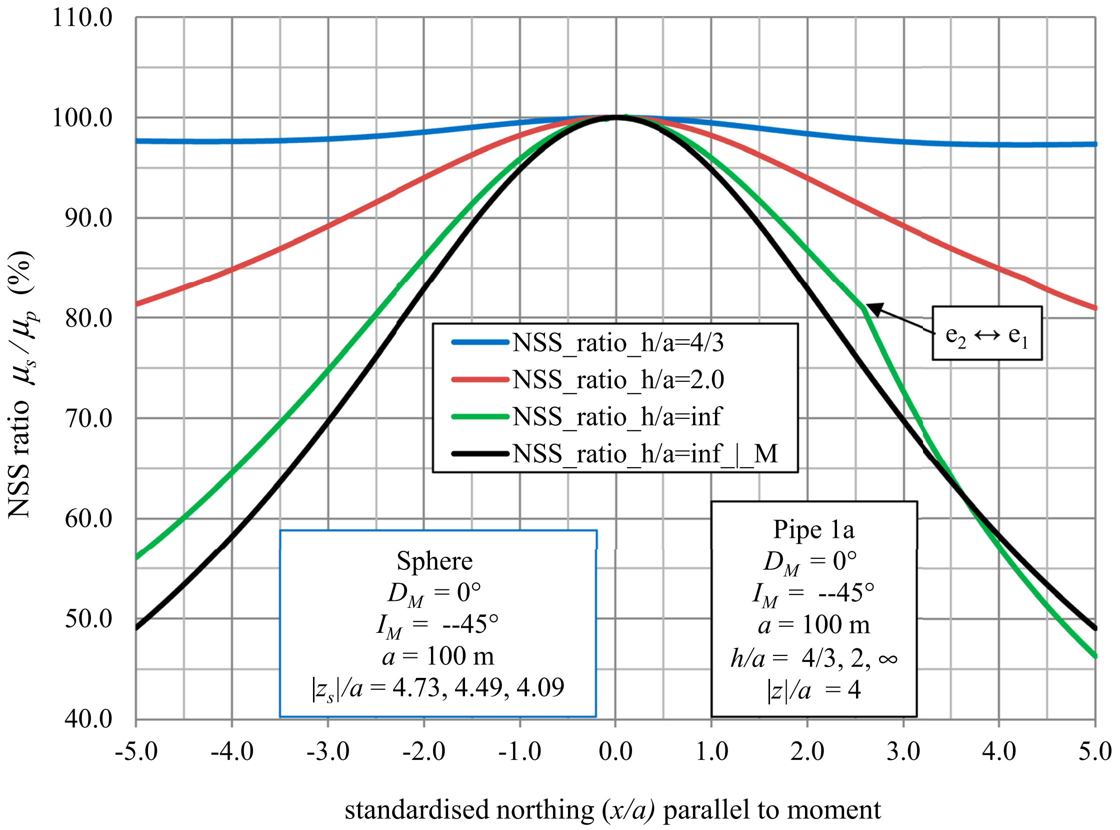

Figure 8. Principal profile plots showing the effect of increasing axial length $h/a = 4/3, 2, \infty$ on the NSS ratios for a series of vertical pipes and their equivalent spheres both with radius $a = 100$ m and inclination of magnetisation $I_M = -45°$ at a standardised observation height $|z|/a = 4$. The symmetric principal profile perpendicular to the direction of magnetisation **M** for $h/a = \infty$ is shown in black.

Table 3. The standardised areal coverage $S_\alpha = (1/a)\sqrt{d_{||}^{\alpha}\, d_{\perp}^{\alpha}}$ based on radial distances $d_{||}^{\alpha}$ and $d_{\perp}^{\alpha}$ to points above a vertical pipe where the NSS ratio $\alpha = \mu_s/\mu_p$ is 95%.

h/a	α_{95} $\lvert z\rvert/a = 1$	α_{95} $\lvert z\rvert/a = 2$	α_{95} $\lvert z\rvert/a = 3$	α_{95} $\lvert z\rvert/a = 4$
4/3	0.375	1.124	3.372	4.435
2	0.362	0.841	1.359	1.795
∞	0.350	0.682	0.906	1.052

to the NSS are dominant (exceeding 90% of the NSS maximum over the full diameter of a vertical pipe) for observation heights $|z|/a \geq 2$. This dominance is more pronounced in compact pipe models and slightly less in the elongated pipes. For standardised observation heights below the radius of the pipe, the dipole contribution to the NSS for the semi-infinite pipe is 65% at $|z|/a = 0.5$ implying the presence of higher order multipole contributions. For these reasons, we conclude that the near field or proximal region for a uniformly magnetised vertical pipe occurs at points where the standardised observation heights $|z|/a < 1$; the far field region for a uniformly magnetised vertical pipe occurs at points where the standardised observation heights $|z|/a \geq 2$ (possibly higher for semi-infinite pipes) and the transition zone between the near and far fields occurs at points where the standardised observation height $1 \leq |z|/a \leq 2$. For this reason (due to the dominance of the dipole component), off-axis estimates of magnetisation direction should improve markedly with increasing observation height in regions where the NSS ratios exceed 90–95 per cent.

5. The three-dimensional symmetric and traceless tensor field of a vertical cylinder: new deliberations for the determination of magnetisation

The NSS provides an excellent means for locating the axial position of a vertical cylinder where both the tensor and its eigenvectors can be used to determine the direction of magnetisation as shown in Table 1. In this section we explore spatial variations in the eigenvalues and vectors in "off -axis" locations with a view to further delineating suitable regions where reliable estimates of magnetisation direction may also be obtained. However there is a complication concerning the interpretation of the eigenvalues of the gradient tensor as revealed in Figure 8, namely, the NSS ratio curve μ_s/μ_p parallel to D_M for the semi-infinite cylinder (green line) displays a clear kink near standardised northing $x/a = 2.5$. This feature results from the fact that the NSS is defined using a fixed ordering of the eigenvalues, so that the eigenvectors associated with λ_1 and λ_2 are swapped at $x/a > 2.5$ due to a degeneracy in the eigenvalue spectrum (i.e. the set of eigenvalues) at this location. This interchange of eigenvectors is not observed in the anti-parallel direction. Furthermore this phenomenon has not been observed or investigated previously for magnetic gradient tensors. In addition to the NSS, new methods are required to pinpoint where degeneracies in the eigenvector field may occur.

5.1. Some recent developments in the study of three-dimensional symmetric and traceless tensor fields

The magnetic and gravity gradient tensors at measurement points external to a source are examples of traceless and symmetric tensors. These traceless tensors whose diagonal elements satisfy Laplace's equation form a subset of three-dimensional symmetric tensor fields. To further investigate the spectral properties of the magnetic gradient tensor of a cylinder, we utilise the visualisation tools developed by Palacios et al. (2016) and Qu et al. (2020), who investigated symmetric tensor fields in both elasticity and fluid dynamics.

A tensor field is a tensor-valued real function defined over three-dimensional (3D) space $\Re^3$. A symmetric rank-2 tensor $\mathbf{T}(\mathbf{r})$ at a point $\mathbf{r} = (x, y, z)^T$ has three real-valued eigenvalues $\lambda_1 \geq \lambda_2 \geq \lambda_3$ which are referred to as the major, medium and minor eigenvalues respectively. When all three eigenvalues are distinct, the tensor is referred to as non-degenerate, otherwise the tensor is termed degenerate. In both cases it is possible to find three right-hand orthonormal eigenvectors $\{\hat{\mathbf{e}}_1, \hat{\mathbf{e}}_2, \hat{\mathbf{e}}_3\}$ such that eigenvector $\hat{\mathbf{e}}_i$ corresponds to eigenvalue λ_i for all $i = 1, 2, 3$.

Palacios et al. (2016) investigate five properties of a symmetric tensor $\mathbf{T}$ which are invariant under a change of basis. These properties are as follows: (1) the trace $I_0 = \lambda_1 + \lambda_2 + \lambda_3$, (2) the minor $I_1 = \lambda_1\lambda_2 + \lambda_2\lambda_3 + \lambda_3\lambda_1$, (3) the determinant $I_2 = \lambda_1\lambda_2\lambda_3$, (4) the tensor magnitude or Frobenius norm $||\mathbf{T}|| = \sqrt{\lambda_1^2 + \lambda_2^2 + \lambda_3^2}$, and (5) the mode

$$\mu_M = \sqrt{6}\frac{\left(\lambda_1 - \frac{I_0}{3}\right)^3 + \left(\lambda_2 - \frac{I_0}{3}\right)^3 + \left(\lambda_3 - \frac{I_0}{3}\right)^3}{\left[\sqrt{\lambda_1^2 + \lambda_2^2 + \lambda_3^2}\right]^3} \tag{28}$$

Note that any symmetric tensor $\mathbf{T}$ can be uniquely decomposed as $\mathbf{T} = \mathbf{D} + \frac{I_0}{3}\mathbf{I}$ where I_0 is the trace of $\mathbf{T}$, $\mathbf{I}$ is the three-dimensional identity matrix and $\mathbf{D}$ is referred to as the deviator matrix of $\mathbf{T}$ (Palacios et al. 2016; Qu et al. 2020). The isotropy index is a measure of the ratio of the strength of isotropy ($I_0/3$) to the strength of anisotropy. For a traceless tensor where $I_0 = 0$, the deviator matrix $\mathbf{D}$ is identical to $\mathbf{T}$, the isotropy index is identically zero and the tensor field of $\mathbf{T}$ is purely anisotropic.

The mode of a traceless tensor is

$$\mu_M = \sqrt{6}\frac{(\lambda_1^3 + \lambda_2^3 + \lambda_3^3)}{\left[\sqrt{\lambda_1^2 + \lambda_2^2 + \lambda_3^2}\right]^3} = 3\sqrt{6}\frac{(I_2)}{||\mathbf{T}||^3}. \tag{29}$$

Degenerate tensors contain repeating eigenvalues and can be identified using the discriminant Δ_T (Palacios et al. 2016):

$$\begin{aligned}\Delta_T &= (\lambda_1 - \lambda_2)^2(\lambda_2 - \lambda_3)^2(\lambda_3 - \lambda_1)^2 \\ &= I_0^2 I_1^2 - 4I_0^3 I_2 - 4I_1^3 + 18 I_0 I_1 I_2 - 27 I_2^2.\end{aligned}$$

which is zero when any of the eigenvalues are identical. For traceless tensors such as the magnetic gradient tensor and the gravity gradient tensor, the invariant I_0 is identically zero so that

$$\Delta_T = -4I_1^3 - 27I_2^2 = 4I_1^3(I - 1),$$

where I is the dimensionless ratio (Pedersen and Rasmussen 1990).

Palacios et al. (2016) define three types of degeneracies, namely, (1) neutral ($\lambda_1 = \lambda_2 = \lambda_3$) or ($\lambda_2 = [\lambda_1 + \lambda_3]/2$) (2) linear ($\lambda_1 > \lambda_2 = \lambda_3$), and (3) planar ($\lambda_1 = \lambda_2 > \lambda_3$). For a linear traceless tensor $\lambda_1 = -2\lambda_2 = -2\lambda_3$ and $\lambda_2 = \lambda_3 < 0$ so that its mode is $\mu_M = 1$ and for a planar traceless tensor $\lambda_3 = -2\lambda_1 = -2\lambda_2$ and $\lambda_1 = \lambda_2 > 0$ so that its mode is $\mu_M = -1$. All three degeneracies are observed in magnetic and gravity gradient tensors. For a dipole, the gradient tensor is neutral only in the plane perpendicular to the moment and is degenerate only along the axis of magnetisation.

Palacios et al. (2016) define the following parameter:

$$\begin{aligned}N = &\left(\lambda_1 - \frac{\lambda_2 + \lambda_3}{2}\right)\left(\lambda_2 - \frac{\lambda_3 + \lambda_1}{2}\right) \\ &\times \left(\lambda_3 - \frac{\lambda_1 + \lambda_2}{2}\right)\end{aligned}$$

For a traceless tensor, N can be written as

$$\begin{aligned}N &= \left(\lambda_1 + \frac{\lambda_1}{2}\right)\left(\lambda_2 + \frac{\lambda_2}{2}\right)\left(\lambda_3 + \frac{\lambda_3}{2}\right) \\ &= \frac{27}{8}\lambda_1\lambda_2\lambda_3 = \frac{27}{8}I_2.\end{aligned}$$

A tensor $\mathbf{T}(\mathbf{r})$ is described as neutral if and only if $N = 0$, i.e. when the medium or second eigenvector $\lambda_2 = \frac{\lambda_3 + \lambda_1}{2}$ (or $\lambda_2 = 0$ for traceless tensors). Neutral points form surfaces in the eigenvector field of a traceless tensor that are associated with locations where the second eigenvalue λ_2, the determinant $I_2 = \lambda_1\lambda_2\lambda_3$ and the mode $\mu_M = 3\sqrt{6}\frac{I_2}{||\mathbf{T}||^3}$ are all zero.

These neutral points partition the eigenvector field of a symmetric tensor $\mathbf{T}(\mathbf{r})$ into major and minor eigenvector fields (Palacios et al. 2016). The major and minor eigenvalues play different roles in the linear and planar regions of the eigenvector field, i.e. where $\lambda_2 <$

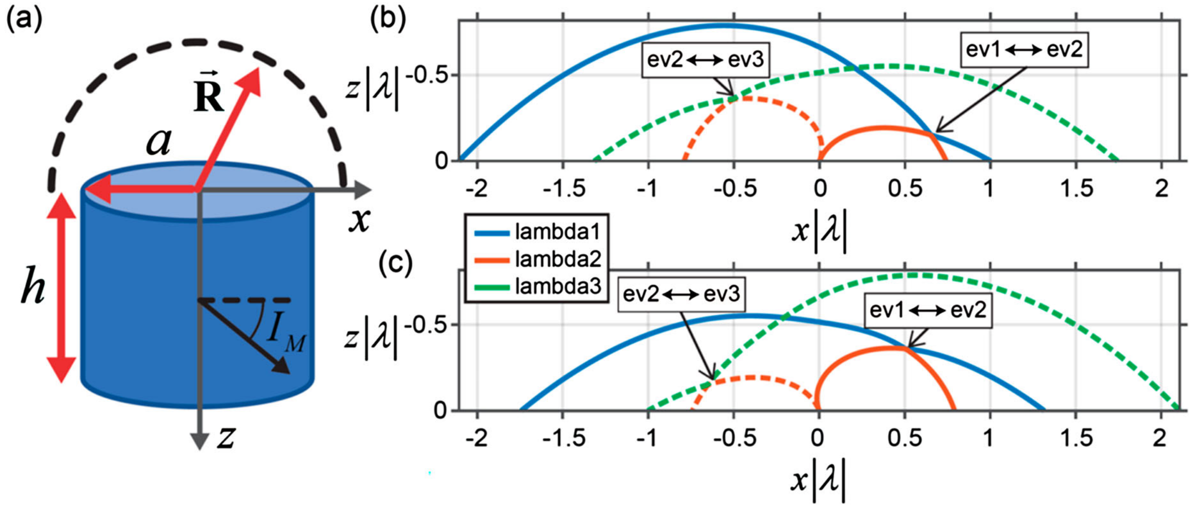

Figure 9. Plots of the eigenvalue surfaces R$|\lambda_i|$; R = (x,z) for a vertical x-z section parallel to the magnetic moment for a uniformly magnetised semi-infinite right circular vertical cylinder with declination of magnetisation $D_M = 0°$ and inclination $I_M = \pm 15°$. Figure 9(b and c) show the eigenvalue surfaces for $I_M = 15°$ and $I_M = -15°$ respectively. Figure 9(a) displays the location of observation points R = (x,z) above a compact right circular cylinder with $h/a = 2$.

$(\lambda_1 + \lambda_3)/2$ and $\lambda_2 > (\lambda_1 + \lambda_3)/2$ respectively, and these roles are reversed or switch across neutral points. More specifically, Palacios et al. (2016) state that for $\lambda_2 < (\lambda_1 + \lambda_3)/2$ or $\lambda_2 < 0$ for traceless tensors, it is the minor or linear eigenvector field which contains interesting topological features in the tensor field which include discontinuities in the eigenvector directions, whereas for $\lambda_2 > (\lambda_1 + \lambda_3)/2$ or $\lambda_2 > 0$ for traceless tensors, it is the major or planar eigenvector field which contains interesting topological features in the tensor field including discontinuities in the eigenvector field.

5.2. Some considerations for the determination of the direction of magnetisation for a right circular cylinder

An important consideration when applying modal analysis to the magnetic gradient tensor for a vertical cylinder is that the eigenvalue fields sometimes intersect at off-axis locations, i.e. where the tensor mode is ±1 and the gradient tensor becomes degenerate. This phenomenon produces spatial discontinuities in the eigenvector components defined by the sorted eigenvalues. These discontinuities arise when a pair of eigenvectors, either $\hat{\mathbf{e}}_2$ and $\hat{\mathbf{e}}_1$ or $\hat{\mathbf{e}}_2$ and $\hat{\mathbf{e}}_3$, swap directions due to spatial changes in the eigenvalues. This phenomenon can be seen clearly in Figure 9 which plots the eigenvalue surfaces along a circular transect above a semi-infinite cylinder. Two eigenvalue surfaces intersect on either side of the cylinder, namely, the λ_2 and λ_3 surfaces intersect on the left side of the central axis while the λ_1 and λ_2 surfaces intersect on the right. At these locations, the ordering of the eigenvalue surfaces changes, which results in a spatial discontinuity in the associated eigenvectors (which are always orthogonal). Furthermore, the scaled radial distance ($x|\lambda|$) to the λ_1, λ_2 intersection point for a southern hemisphere magnetisation $I_M = -15°$ (Figure 9(c)) is identical to that for the λ_2, λ_3 intersection for a northern hemisphere magnetisation $I_M = 15°$ (Figure 9(b)). These distances interchange for the same inclinations I_M in opposite hemispheres.

The three eigenvalues for a dipole or magnetic sphere all scale as $\lambda \propto r^{-4}$ and are not discontinuous (Clark, 2012). In this regard, the eigenvalue surfaces for a vertical cylinder are markedly different to that of a dipole in that they are highly asymmetric and display multiple crossovers. Therefore it may be concluded (or is highly likely) that the crossovers in the eigenvalues are actually indicative of the presence of non-dipole field components in the magnetic field of a vertical cylinder or pipe.

Figure 10 shows principal profile plots parallel to the direction of magnetisation or magnetic moment at a standardised observation height $|z|/a = 0.5$ above a semi-infinite right circular vertical cylinder of radius $a = 10$ m and magnetisation direction $D_M = 0°$, $I_M = 15°$. Figure 10(a and b) show the relative location of crossover points where the $\hat{\mathbf{e}}_2$, $\hat{\mathbf{e}}_3$ and $\hat{\mathbf{e}}_2$, $\hat{\mathbf{e}}_1$ eigenvector pairs interchange direction. These relative locations are expressed in standardised radial coordinates (x/a), i.e. the signed distance from the central axis of the pipe. Points where the second and third eigenvectors interchange, denoted $\hat{\mathbf{e}}_2 \leftrightarrow \hat{\mathbf{e}}_3$, are delineated by simultaneous maxima in the ratio λ_2/λ_3 and the mode μ_M and minima in the ratio λ_2/λ_1 which all occur on the southern side of the vertical pipe (antiparallel to $D_M = 0°$) at a standardised radial distance $x/a = -3.10 \pm 0.05$. Furthermore, points where the $\hat{\mathbf{e}}_2$, $\hat{\mathbf{e}}_1$ eigenvectors interchange are delineated by a maximum in the ratio λ_2/λ_1 and minima in the mode μ_M and the ratio λ_2/λ_3 which all occur on the northern side of the vertical pipe (parallel to D_M) at

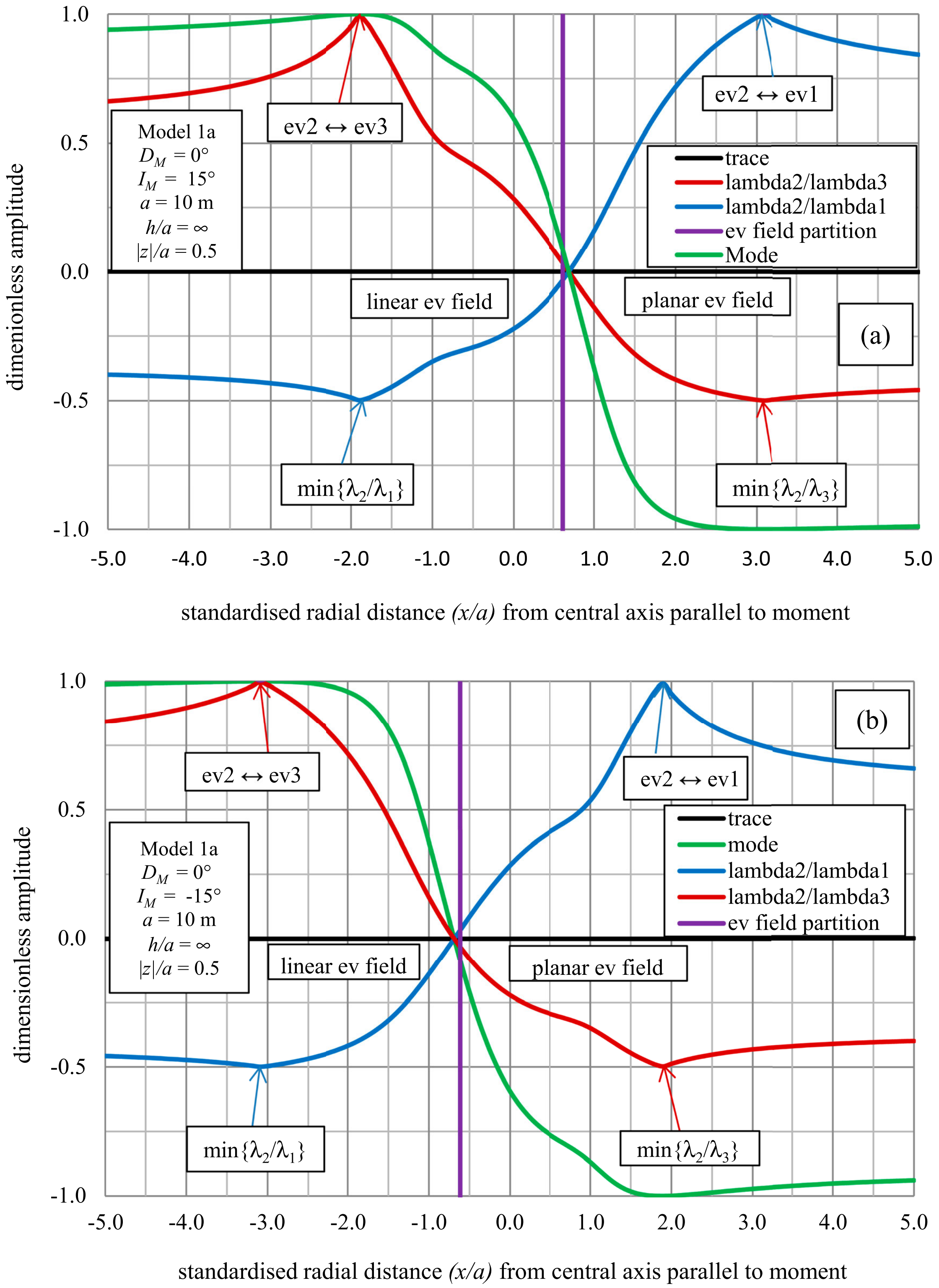

Figure 10. Principal profiles for λ_2/λ_1, λ_2/λ_3, the mode μ_M and the neutral or zero mode partition points of the eigenvector field for a semi-infinite vertical cylinder. Figure 10(a) shows these principal profiles for a northern hemisphere magnetisation $I_M = 15°$ while Figure 10(b) shows the same principal profiles for a southern hemisphere magnetisation $I_M = -15°$. The standardised observation height is $|z|/a = 0.5$ in both cases.

$x/a = 1.80 \pm 0.05$. The positions of the $\hat{\mathbf{e}}_1 \leftrightarrow \hat{\mathbf{e}}_2$ and $\hat{\mathbf{e}}_2 \leftrightarrow \hat{\mathbf{e}}_3$ crossover points are equidistant from the neutral partition points in the eigenvector field where the mode μ_M is zero.

For magnetisations in both hemispheres, i.e. $-90° \leq I_M \leq 90°$, the $\hat{\mathbf{e}}_2 \leftrightarrow \hat{\mathbf{e}}_3$ crossover occurs in the major or linear eigenvector field of the gradient tensor where the mode μ_M is 1. In contrast, the crossover between $\hat{\mathbf{e}}_2 \leftrightarrow \hat{\mathbf{e}}_1$ occurs in the minor or planar eigenvector field of the gradient tensor where the mode μ_M is -1. The partition between major and minor eigenvector fields is marked by neutral points in the tensor field where both λ_2 and the mode μ_M are zero (Palacios et al. 2016). This is shown in Figure 10(a and b) where the zero

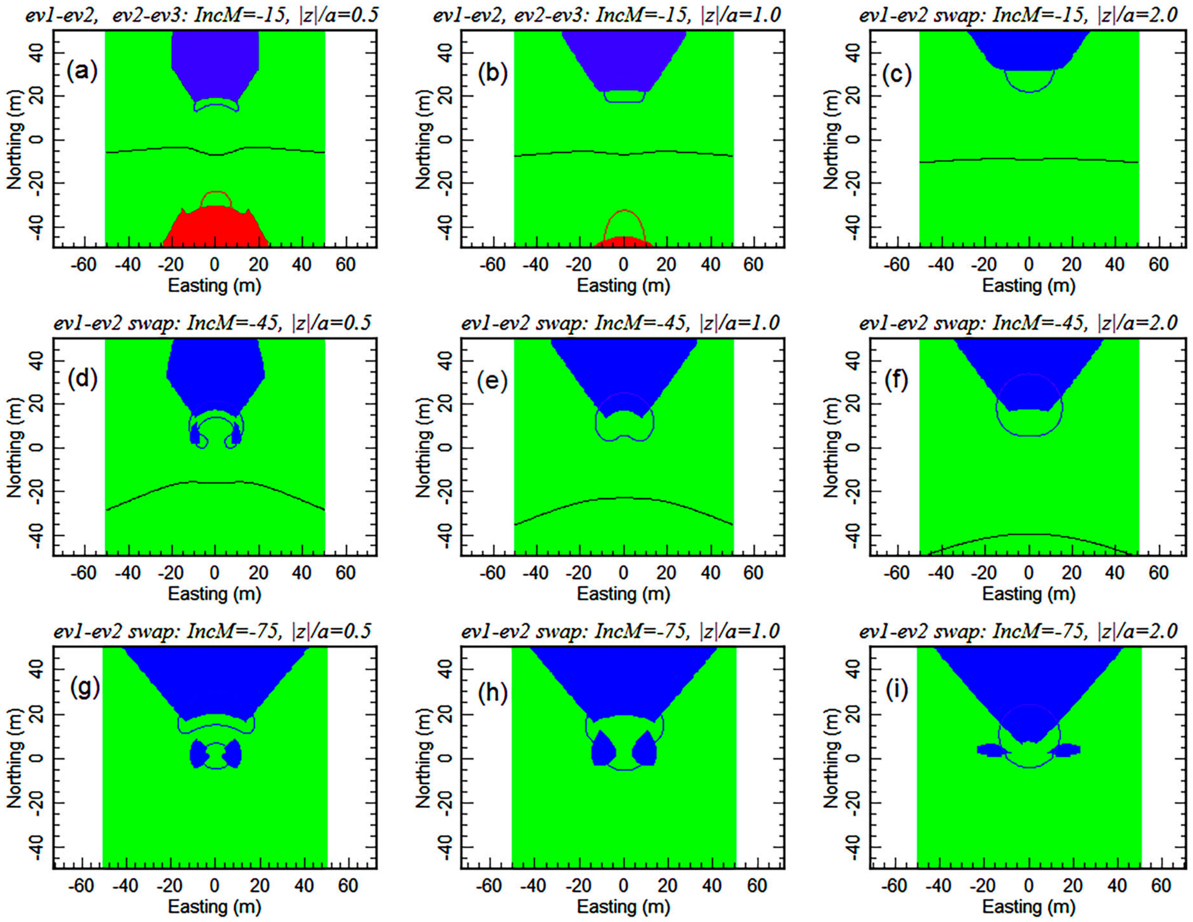

Figure 11. Grid images (100 × 100 m) showing regions where the first $\hat{e}_1$ and second $\hat{e}_2$ eigenvectors (shown in blue) and where the second $\hat{e}_2$ and third $\hat{e}_3$ eigenvectors (shown in red) have interchanged directions for a series of semi-infinite vertical pipe models of radius $a = 10$ m, and inclination of magnetisation $I_M = -15°, -45°, -75°$. The standardised observation heights are $|z|/a = 0.5, 1.0, 2.0$ in each of the three magnetisation directions (declination $D_M = 0°$). The mode zero contour is shown in black in Figure 11(a–f), and the ±0.99 mode contours are shown in blue and red respectively.

crossings of λ_2/λ_3, λ_2/λ_1, and the mode μ_M all intersect at $x/a = \pm 0.70 \pm 0.05$.

The delineation of regions where eigenvectors pairs $\hat{\mathbf{e}}_1 \leftrightarrow \hat{\mathbf{e}}_2$ or $\hat{\mathbf{e}}_2 \leftrightarrow \hat{\mathbf{e}}_3$ have interchanged involve the off-axis tracking of eigenvector $\hat{\mathbf{e}}_2$ in conjunction with the detection of global maxima in λ_2/λ_1 or λ_2/λ_3 when the mode μ_M is -1 or 1 respectively. This methodology has been applied to a series of semi-infinite vertical pipe models of radius $a = 10$ m, declination of magnetisation $D_M = 0°$, and inclination of magnetisation $I_M = -15°, -45°, -75°$ (Pipe model 1b). Since the direction of the second eigenvector $\hat{\mathbf{e}}_2$ is known at axial points above a cylinder, i.e. $\hat{\mathbf{e}}_2 = (0, 1, 0)$, then $\hat{\mathbf{e}}_2$ can be tracked along principal profiles parallel to the direction of magnetisation D_M using expressions shown in Table 1. This is illustrated in Figure 11 which shows a series of grid images (with range $x/a = \pm 5$, $y/a = \pm 5$) and standardised observation heights $|z|/a = 0.5, 1.0, 2.0$. Locations where the first $\hat{\mathbf{e}}_1$ and second $\hat{\mathbf{e}}_2$ eigenvectors have swapped are plotted in blue and locations where the second $\hat{\mathbf{e}}_2$ and third $\hat{\mathbf{e}}_3$ eigenvectors have swapped are plotted in red. Regions where the direction of the second eigenvector remains continuous are shown in green.

Note that the $\hat{\mathbf{e}}_2 \leftrightarrow \hat{\mathbf{e}}_3$ crossover regions are only present for $I_M = -15°$ and $|z|/a \leq 1.0$ (Figure 11(a and b)). The images in Figure 11 demonstrate that the eigenvector fields of a semi-infinite right circular vertical pipe are strongly influenced by the direction of magnetisation and the standardised observation height $|z|/a$.

To illustrate this further, Figure 12 shows the location of neutral partition points in the eigenvector field i.e. where the mode $\mu_M = 0$ for a series of principal profiles at varying heights above a right circular vertical pipe in which the inclination of magnetisation I_M is varied from −45°N to 45°N in steps of 15°.

For magnetisations in the northern hemisphere, $I_M > 0°$, the neutral partition points in the eigenvector field migrate outwards with increasing I_M along the direction of magnetisation $D_M = 0°$, whereas for magnetisations in the southern hemisphere, i.e. $I_M < 0°$, the neutral points migrate outwards but in the opposite direction. For steep magnetisations, i.e. $|I_M| > 45°$ in either hemisphere, the neutral points in Figure 12 occur outside the standardised radial distance $x/a = \pm 5.0$. The location of neutral partition points in the eigenvector field for pairs of magnetisations in opposite

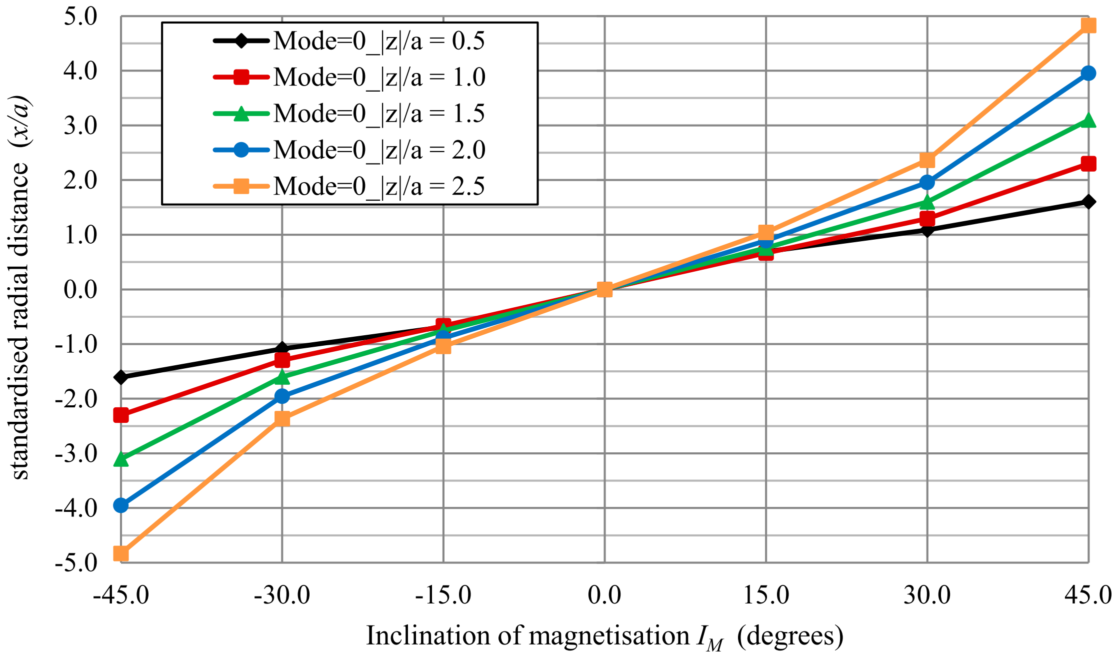

Figure 12. Plots which show the relative location of neutral points in the eigenvector field for a series of principal profiles parallel to the declination of magnetisation $D_M = 0°$ at varying heights $|z|/a = 0.5$–2.5 above a right circular vertical pipe. The effect of changing inclination of magnetisation $I_M = -45°$ to $45°$ is shown for each observation height.

hemispheres is antisymmetric about the central axis of a vertical cylinder. This symmetry in the distribution of neutral points in the eigenvalue manifold is repeated for all standardised observation heights $0.5 \leq |z|/a \leq 2.5$ and inclinations of magnetisation on the range $-45° \leq I_M \leq 45°$ as shown in Figures 10 and 12.

Figure 13 shows the relative location of $\hat{\mathbf{e}}_2 \leftrightarrow \hat{\mathbf{e}}_1$ crossover points along principal profiles parallel to D_M for a series of magnetisations in the southern hemisphere, i.e. $I_M = -75°$ to $0°$. The $\hat{\mathbf{e}}_2 \leftrightarrow \hat{\mathbf{e}}_3$ crossover points for a series of magnetisations in the northern hemisphere $I_M = 0°$ to $75°$ occur at the same radial distances from the axis but antiparallel to D_M. Therefore the relative positions of the $\hat{\mathbf{e}}_1 \leftrightarrow \hat{\mathbf{e}}_2$ and $\hat{\mathbf{e}}_2 \leftrightarrow \hat{\mathbf{e}}_3$ crossovers are mirror images of each other for the same inclination of magnetisation in opposite hemispheres. It is further noted that there are no eigenvector crossovers for an axially magnetised vertical cylinder, i.e. for $I_M = \pm 90°$, which has a smoothly varying eigenvector field akin to that of a point magnetic pole.

In summary these observed anti-symmetries in the eigenvector crossover points exist for all pairs of magnetisations (with a non-zero horizontal component) in either hemispheres and for all observation heights (Figure 13). Understanding this complexity in the eigenvector field including knowledge of where crossovers in the $\hat{\mathbf{e}}_2 \leftrightarrow \hat{\mathbf{e}}_1$ and $\hat{\mathbf{e}}_2 \leftrightarrow \hat{\mathbf{e}}_3$ eigenvectors may occur is essential to defining regions where we can successfully estimate the direction of magnetisation over a uniformly magnetised cylinder.

6. Determination of magnetisation direction from gradient tensor survey data over a reversely magnetised pipe-like anomaly from the Diavik diamond field

The feasibility of using our new tensor based methods to determine the direction of magnetisation of a vertical cylinder is tested using gradient tensor data collected over a pipe-like anomaly from the Diavik diamond field. The Diavik diamond field lies about 300 km northeast of Yellowknife in the Northwest Territories of Canada (see Figure 14). The Lac de Gras kimberlites were intruded into late Archean rocks of the Slave Geological Province (Graham et al. 1999). The Lynx-A154 kimberlites possess a reverse natural remanent magnetisation (NRM) carried by single domain Ti-bearing magnetite which produces significant negative TMI anomalies (Graham et al. 1999; Lockhart, Grütter, and Carlson 2004). Radiometric Rb-Sr isotopic dating of the A154 phlogopite bearing kimberlites shows clustering at 55.4 ± 0.4 Ma which corresponds to the Chron C25n reverse palaeopole (Lockhart, Grütter, and Carlson 2004). This makes these pipes ideal candidates for a tensor analysis.

6.1. The magnetic gradient tensor survey

Full magnetic gradient tensor data have been acquired by Rio Tinto Exploration (RTX) over a (1 km × 1 km) region to southeast of Lac de Gras. The gradient tensor data comprising elements B_{xx}, B_{xy}, B_{xz} B_{yy}, B_{yz}, and B_{zz}, were acquired by helicopter survey at a flight height of

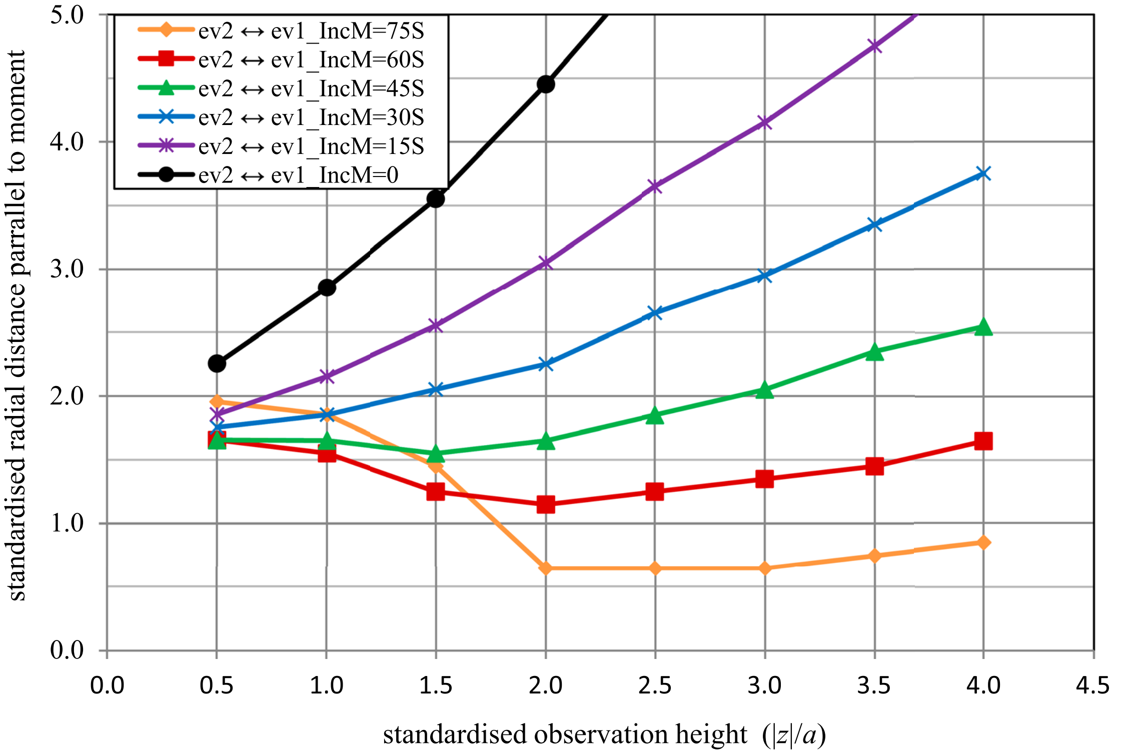

Figure 13. Plots of the relative location of crossover points in the eigenvector field for a series of principal profiles parallel to D_M at varying heights from $|z|/a = 0.5$ to 4 above a right circular vertical cylinder in which the inclination of magnetisation is varied from −75° to 0°.

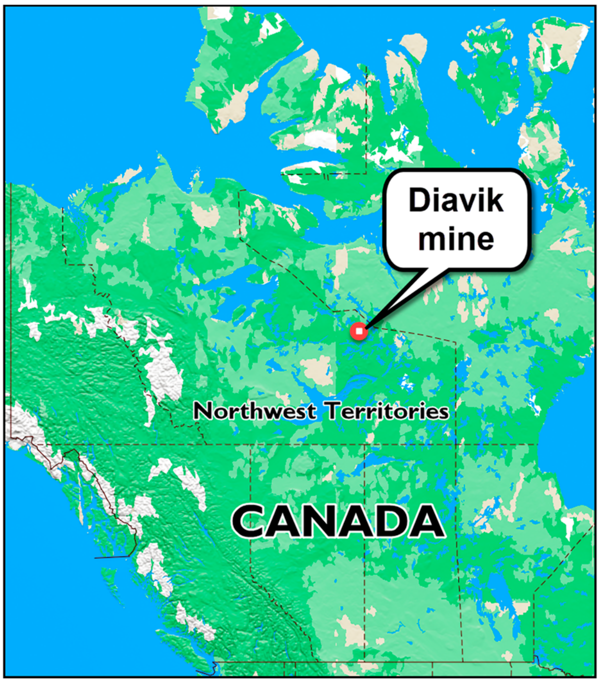

Figure 14. Locality map for the Diavik diamond field.

30–35 m with an in-line sampling interval of 2.5 m and a line spacing of 50 m.

The NSS data are computed directly from the eigenvalues of the acquired gradient tensor data. Figure 15 shows contoured images and stacked profiles of the NSS for a selected region of survey data. This region contains a strongly magnetised north-east trending dyke-like structure and several isolated pipe-like anomalies some of which have reverse magnetisations, shown as dark shading in the B_{zz} stacked profiles in Figure 15. In particular, Figure 15 shows two closely spaced, pipe-like anomalies designated as anomalies A and B on lines 11150 and 11200 respectively. Both pipe-like bodies possess reverse magnetisation characterised by strongly negative B_{zz} anomalies.

Anomaly A has been selected for analysis of magnetisation direction. A segment of gradient tensor B_{xz}, B_{yz}, B_{zz}, and NSS data are plotted in Figure 16. The upward continued NSS maximum for anomaly A is $\mu_{\text{max}} =$ 6.545 nT/m which is located on line 11150 at 547457.61E, 7147621.19N at a line distance of 1157.5 m.

There is slight asymmetry in the B_{zz} and NSS data which suggest that line 11150 is not orthogonal to the direction of magnetisation (see Appendix 3) There is also evidence of interference to the west of anomaly A. Finally, the B_{xz} and B_{yz} tensor elements display a constant DC shift, possibly related to constant background noise.

6.2. Interpretation of the survey gradient tensor data

Table 4 shows the location, body properties and magnetisation derived from the gradient tensor data at the NSS maximum on line 11150. The B_{zz} data in Figure 16 indicate that anomaly A has strong reverse remanent magnetisation with Koenigsberger ratios $Q = M_{nrm}/M_{ind}$ significantly greater than 1.

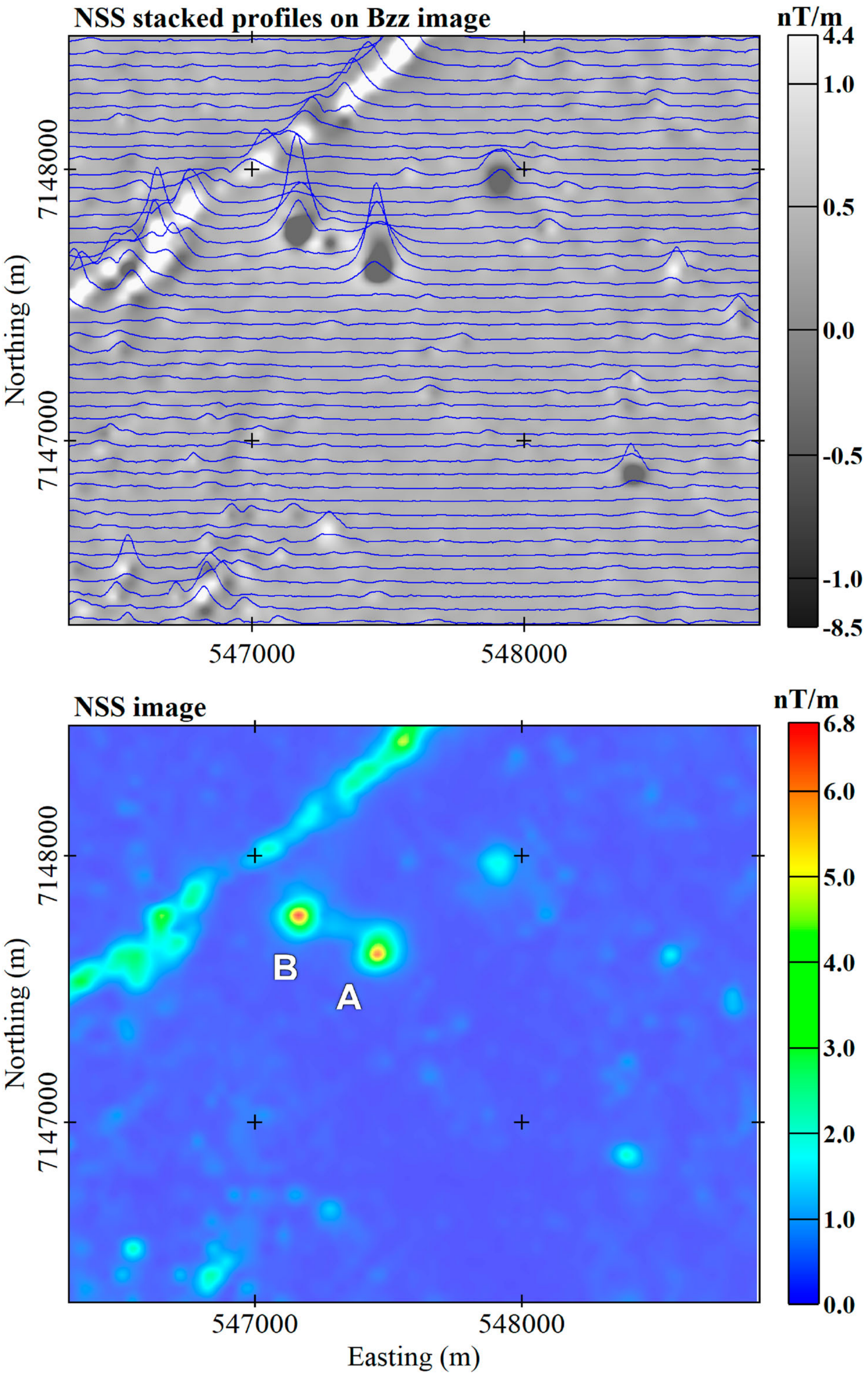

Figure 15. Stacked profiles of the NSS line data (shown in blue) with grey scale shading of B_{zz} and coloured images of the NSS upward continued 6 m for a selected region of the Diavik survey area.

An estimate of the elevation above centre $|z|$ at the NSS maximum is obtained from the radar altimeter data in Table 4. This estimate provides an initial lower bound depth to the top of the glaciated surface for pipe anomaly A. The NSS profile in Figure 16 displays a unimodal peak over the centre of anomaly A which is consistent with a standardised observation height $|z|/a > 1$, implying that this is also the centre of the body. This interpretation is further supported by the difference between the inclinations of the first and third eigenvectors $I_{ev3} - I_{ev1}$ in Table 4 which is close to the theoretical value of 90° on the axis of a vertical cylinder.

Reliable estimates for the diameter of a vertical pipe at standardised observation heights $|z|/a$ below 1.5 can be obtained from the distance between the maxima and minima in B_{xz} or B_{yz} (depending on which is the greater) with an estimated accuracy within ±10% for

Table 4. Body properties and magnetisation directions (as defined in Table 1) derived from gradient tensor data at the NSS maximum on line 11150 for Diavik pipe anomaly A.

Pipe Model Parameter	Magnetisation results anomaly A Line 11150
$\mu_{\max}$ (nT/m)	8.422
xtc top centre (m)	7147621.82N
ytc top centre (m)	547457.60E
line distance (m)	1157.50
radar-altimeter (m)	34.50
a (m)	27.50
h (m)	150.00
$\lvert z \rvert$ (m)	34.50
$\lvert z \rvert / a$	1.25
h/a	5.45
M (A/m)	3.09
D_M (from D_{mgt})	024.85°
I_M (from I_{mgt})	−63.17°
D_M (from D_{ev1})	103.41°
D_M (from D_{ev3})	023.26°
I_M (from ϕ−90°)	−26.46°
$I_{ev3} - I_{ev1}$	81.61°

Note: The parameters D_{mgt}, D_{ev1}, D_{ev3} are declinations of magnetisation D_M obtained from the gradient tensor (mgt), and the first and third eigenvectors. Similarly, I_{mgt} and $I_{\phi-90}$ are the inclinations of magnetisation computed from the the gradient tensor and ϕ− 90°. Finally, I_{ev1} and I_{ev3} are inclinations of the first and third eigenvectors.

$|z|/a \leq 1.5$. Using this approach, the radius for anomaly A has been estimated as $a = 27.5$ m from the profile plot of tensor element B_{yz} in Figure 16. The estimates of radius and depth enable computation of the standardised observation height $|z|/a$ which is approximately 1.25 for this anomaly (see Table 4). This standardised height is also consistent with the measured NSS half widths for a vertical pipe in Figure 16 (see Table 4 and Appendix 3).

6.3. Notes on the eigenvector field for anomaly A

Figure 17 confirms that anomaly A has gradient tensor elements which lie in the planar eigenvector field, i.e. $-1 < \mu_M < 0$ between 1052.5 and 1282.5 m on line 11150 m. No crossovers of the $\hat{\mathbf{e}}_2$ and $\hat{\mathbf{e}}_1$ eigenvectors occur within this range, i.e. where both λ_2/λ_1 and the tensor mode μ_M have simultaneous minima near −1. The NSS data are high quality and smoothly varying for all points in anomaly A where the relative NSS $\mu/\mu_{\max} > 0.25$. For anomaly A west of 1050 m, the eigenvector field changes to linear $0 < \mu_M < 1$ with a simultaneous peak for both λ_2/λ_3 and the mode $\mu_M = 0.997$ between 1002.5 and 1005 m. This is consistent with a crossover of the $\hat{\mathbf{e}}_2$ and $\hat{\mathbf{e}}_3$ eigenvectors and marks the first time that this phenonemon has been observed in real data. In summary, the gradient tensor data on line 11150 satisfy criteria for estimation of magnetisation direction over the NSS peak. This will be further tested by joint inversion of the full gradient tensor at points where $\mu/\mu_{\max}$ exceeds the background level of 0.25 in Figure 17.

6.4. Determination of magnetisation directions at the NSS peak

Table 4 shows the intensity of magnetisation M and the magnetisation directions derived from the survey tensor data for anomaly A. The declination D_M and inclination of magnetisation I_M are estimated from the gradient tensor elements using Equations (A2.5) and (A2.6) respectively in Appendix 2 (see also Table 1). The intensity of magnetisation M is estimated from $M = \mu/\beta$ where β has been calculated from Equation (4)

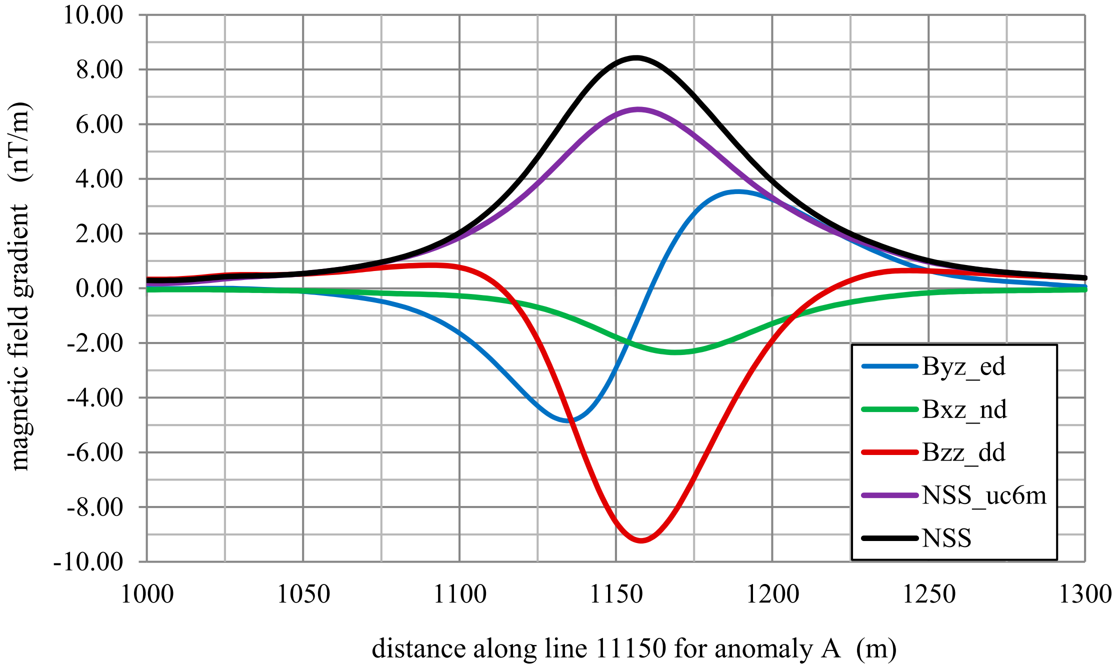

Figure 16. Gradient tensor and NSS line data profiles for pipe anomaly A on survey line 11150. The local geomagnetic field has intensity 58153 nT, declination 12.2°, and inclination 82.2°.

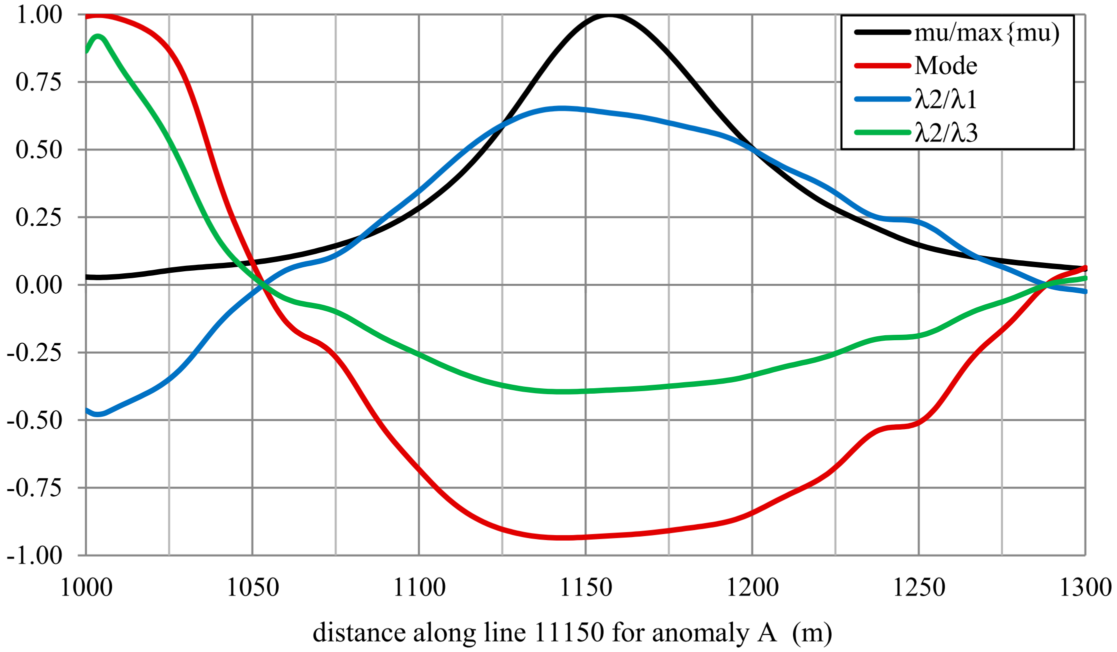

Figure 17. Plots showing the relative NSS ($\mu/\mu_{\max}$), the tensor mode μ_M, and the eigenvalue ratios λ_2/λ_1 and λ_2/λ_3 for pipe anomaly A on line 11150. The vertical axis is dimensionless.

using estimates of $|z|/a$ and h/a in Table 4. Alternatively the declination D_M of magnetisation may be estimated from the declinations of the first and third eigenvectors D_{ev1} and D_{ev3}. The inclination of magnetisation I_M may be estimated from $\mu_{\max}$ and the second eigenvector λ_2 using Equation (12), i.e. $I_M = \phi - \pi/2$ where $\phi = \arccos(\lambda_2/\mu_{\max})$. At this point we note that the NSS survey peak may not correspond to the actual position of the NSS maximum which may be located between a pair of survey lines. Hence the estimates of magnetisation direction from the gradient tensor in this instance can be offset from the centre of the pipe. How far "off-axis" is determined by the survey line spacing and the diameter of the pipe. This difficulty can be partly resolved by inversion in which the starting model parameters are defined from the survey NSS peak.

The estimates of D_M for pipe anomaly A computed from the gradient tensor D_{mgt} and from the principal eigenvector D_{ev3} at the NSS peak are in close agreement, namely, $D_{mgt} = 024.85°$ and $D_{ev3} = 023.26°$. The inclination of magnetisation I_M estimated from the gradient tensor is $I_{mgt} = -63.2°$, while I_M from the maximum NSS using $I_M = \phi - 90°$ is significantly lower, i.e. $I_{\phi-90°} = -26.5°$. In addition, there are discrepancies between $D_{ev1} = 103.4°$ and the average estimate of declination $D_M = 024.05 \pm 0.2°$.computed from D_{mgt} and D_{ev3}. The exact cause of this discrepancy between D_{ev1} and D_{ev3} is unclear because these estimates are usually in close agreement for synthetic model data (McKenzie 2020). The lower estimates of inclination from $I_{\phi-90°}$ could be due to background noise in the second eigenvector λ_2 which is associated with the lowest absolute value of the three eigenvalues, and therefore, the lowest signal to noise ratio. Despite this discrepancy in the inclination estimates, the results in Table 4 confirm that pipe anomaly A possesses a strong reverse remanent magnetisation with high Koenigsberger ratios and total magnetisation intensity M close to 3.1 $\mathrm{Am^{-1}}$. As an example, for a magnetic susceptibility of 0.01 SI units, the Koenigsberger ratio at the NSS peak in Table 4 is 7.5, and the remanent magnetisation has an intensity of $M_{nrm} = 3.48\ \mathrm{Am^{-1}}$ with declination $D_{nrm} = 024.6°$ and inclination $I_{nrm} = -67.5°$.

6.5. Comparison with inversion results

To test the veracity of the different approaches, we can compare these results with a formal parameter inversion using a starting model based on the NSS peak analysis. Table 5 shows results derived from a non-linear parametric inversion (Pratt and McKenzie 2009) of full gradient tensor data over selected data ranges from 1075 to 1235 m on line 11150 for anomaly A.

This data range for the inversion covers the sweet spot (i.e. $\mu/\mu_{\max} > 0.25$) for anomaly A shown in Figure 17. The forward models for the parametric inversions use expressions for the six gradient tensor elements of a uniformly magnetised right circular vertical cylinder (McKenzie 2022). Model parameters for the inversion are top centre position, i.e. xtc, ytc, ztc, radius a, magnetisation intensity M and the declination D_M and inclination I_M of the total magnetisation vector **M**. The axial length h was fixed at 150 m or $h/a = 5.45$.

The inversion for anomaly A in Table 5 has been performed on the full gradient tensor with results obtained by the removal of a tensor consistent DC offset in each of the six tensor channels. Table 5 shows the final model

Table 5. Parametric joint inversion results for pipe anomaly A on line 11150.

Pipe Model Parameter	Survey NSS results Line 11150 Anomaly A	DCO Inversion. Results Line 11150 Pipe anomaly A	Model differences after inversion Pipe anomaly A
xtc top centre (m)	7147621.82N	7147621.89N	0.07
ytc top centre (m)	547457.60E	547459.28E	1.68
ztc-down (m)	0.00	3.73	3.73
radar-altimeter (m)	34.50	34.50	0.00
a (m)	27.50	24.57	−2.93
h (m)	150.00	150.00	0.00
$\|z\|$ (m)	34.50	38.23	3.73
h/a	5.46	6.11	0.65
$\|z\|/a$	1.25	1.56	0.31
M (A/m)	3.09	2.61	0.48
D_M (inversion seed)	025.00°	024.54°	−0.46°
I_M (inversion seed)	−63.00°	−63.89°	−0.89°
D_M (from D_{mgt})	024.85°	019.29°	−5.56°
I_M (from I_{mgt})	−63.17°	−64.71°	−1.54°
D_M (from D_{ev1})	103.41°	023.22°	−80.19°
D_M (from D_{ev3})	023.26°	019.20°	−4.07°
I_M (from ϕ−90°)	−26.46°	−64.27°	−37.81°
$I_{ev3} - I_{ev1}$	81.61°	89.98°	8.37°

Note: The starting parameters for the inversion are identical to those derived from the gradient survey data at the NSS peak. The modelled magnetisation directions from the best inversion model are shaded in beige. The average normalised RMS error from the final model was 8.54% and the best estimated DC offsets for B_{xx}, B_{xy}, B_{xz}, B_{yy}, B_{yz}, and B_{zz} were 0.401, −0.0169, −0.0255, −0.637, 0.0320 and 0.235 nT/m respectively.

parameters and their change from the starting model for xtc, ytc, ztc, a, M, D_M, and I_M. The geometric parameters xtc, ytc which define the horizontal centre of magnetisation show little variation from the initial parameters derived from the peak NSS. This implies that the NSS maximum lies close to the true horizontal centre of magnetisation for pipe anomaly A. The radius a has decreased by 10.65% and the depth parameter |z| has increased by 10.8% so that |z|/a has increased by 24.8% to 1.56. The intensity of magnetisation M obtained from the inversion has decreased from 3.09 $\mathrm{Am^{-1}}$ to 2.61 $\mathrm{Am^{-1}}$. The best model parameters from the inversion are then used to calculate the direction of magnetisation parameters D_{mgt}, I_{mgt}, D_{ev1}, D_{ev3}, and I_M (ϕ−90°) from the modelled gradient tensor and NSS.

The magnetisation directions from the inversion in Table 5 show good agreement with the results obtained from the NSS peak in Table 4. The average declination for anomaly A in Table 5 is 021.56° ± 2.73° compared with the average $D_M = 024.06° \pm 0.80°$ (from D_{mgt} and D_{ev3}) at the NSS peak. The inclination results obtained from the inversion and from the modelled gradient tensor are −63.89° and −64.49° ± 0.22 respectively, which agree closely with $I_{mgt} = -63.17°$ at the NSS maximum. The inversion results in Table 5 suggest that the declination estimate D_{ev3} from the third or principal eigenvector, which, for a southern hemisphere magnetisation, has the largest eigenvalue magnitude, may provide more consistent estimates of D_M than those calculated from the first eigenvector D_{ev1}.

The intensity and direction of remanent magnetisation and Koenigsberger ratio for the Diavik pipe anomaly may be calculated from the total resultant magnetisation results in Table 5 using reliable susceptibility measurements. This enables comparisons between the magnetic inclination of the palaeopole with estimates of the inclination of remanent magnetisation I_{nrm} calculated from the results in Table 5. The magnetic survey data for anomaly A suggest moderate to high magnetic susceptibilities, high NRM intensities and high Koenigsberger (Q) ratios. For magnetic susceptibilities ranging from 0.001 to 0.015 SI, the intensities of remanent magnetisation increase from $M_{nrm} = 2.65$ to 3.21 $\mathrm{Am^{-1}}$, the inclination of remanent magnetisation I_{nrm} steepens from −64.5° to −70.8° and the Q ratios decrease from 57.2 to 4.62. These inclinations correspond to a palaeolatitude ranging from −46.28° to −55.12°. Based on a plate reconstruction, the position of the Diavik site for an assumed age of 55 Ma (the Chron C25n reversal period) is latitude −67.62°, longitude −83.24° which implies a discrepancy of 12.5° in the inclination of the inferred palaeopole (Müller et al. 2019). We conclude that the palaeopole reversal at Chron C25n generally supports the steep reverse inclination of magnetisation for the Diavik pipe anomaly. Furthermore our NRM results are broadly consistent with some published palaeomagnetic data for several Diavik kimberlite pipes (Lockhart, Grütter, and Carlson 2004).

In summary, inversion of the gradient tensor for pipe anomaly A has provided consistent estimates of magnetisation which are in broad agreement with those determined at the NSS peak in Table 4. Additional research is required to quantify the effects of noise on the parameter estimates as well as any effects caused by geometric deviations from a perfect cylinder. However, the results in this section clearly demonstrate that reliable estimates of magnetisation direction can be obtained at the NSS peak using the gradient tensor, its NSS and at least one of the eigenvectors.

7. Conclusions and future work

This paper presents some new insights into the nature and complexities of the eigenvector fields of a right circular vertical cylinder. This knowledge may be used to determine the magnetisation direction above isolated pipe-like magnetic anomalies. The main research findings are as follows.

First, analytical expressions on the axis of a uniformly magnetised, semi-infinite or finite length, right circular vertical cylinder have been presented for the three eigenvalues, the NSS, the inclination of magnetisation and some important tensor invariants. These expressions are identical in form to those obtained by Clark (2012) for an observation point located above a magnetic dipole or magnetic sphere. Several expressions for the declination of magnetisation D_M on the cylinder axis are derived from the three eigenvectors $\hat{\mathbf{e}}_1$,$\hat{\mathbf{e}}_2$, $\hat{\mathbf{e}}_3$ of the magnetic gradient tensor. These expressions yield the same declination of magnetisation as obtained from the magnetic field components and magnetic gradient tensor.

Second, the NSS of a right circular vertical cylinder is strongly influenced by the direction of magnetisation, the standardised observation height $|z|/a$, and the shape factor h/a. The NSS shows an azimuthal asymmetry not present for point pole or dipole sources. Analysis of the magnetic potential showed that all the asymmetry is due to the horizontal (or radial) component of magnetisation, whereas the vertical component of magnetisation produces radial symmetry akin to that of a dipole or point pole. For this reason, maximum asymmetry occurs in the NSS either parallel or antiparallel to the declination of magnetisation whereas symmetric or anti-symmetric properties are found perpendicular to it. This azimuthal asymmetry in the NSS lessens with increasing observation height as does the influence of the shape factor h/a so that the NSS over a pipe can be modelled as a dipole for $|z| > 2a$.

Third, this investigation of the NSS has shown that the proximal or near field region of a vertical pipe occurs at observation heights below half the diameter of the pipe, i.e. for $|z| < a$. In this region non-dipole components are clearly present in the tensor field. As a result, the NSS no longer peaks on the axis of a vertical cylinder. Rather, the NSS maxima are situated on or inside the rim of the cylinder along a line parallel or antiparallel to the direction of magnetisation. The distal or far field region is dominated by the dipole component, and, for a vertical cylinder, this region occurs at points which lie directly above its top surface at observation heights which exceed its diameter, i.e. $|z| > 2a$. The transition between the near- and far field appears to be in the region where the observation height lies from $a < |z| < 2a$. We conclude that it is in these transitional and far field regions over a sweet spot anomaly that are best suited to accurate determinations of magnetisation and magnetisation direction.

Fourth, neutral surfaces in the eigenvector field of the traceless magnetic gradient tensor occur when the second eigenvalue λ_2 and the tensor mode μ_M are zero. These neutral surfaces partition the eigenvector field into major and minor eigenvector fields. In agreement with Palacios et al. (2016), these major and minor eigenvector fields contain significant topological features including crossovers in the eigenvalue surfaces which produce spatial discontinuities in the eigenvector fields. This is attributable to the ordering of the three eigenvalues of the magnetic gradient tensor as is used to define the NSS. Points of linear degeneracy (mode $\mu_M = 1$) and planar degeneracy (mode $\mu_M = -1$) within the major and minor eigenvector fields respectively, delineate boundaries where pairs of eigenvectors crossover, namely, $\hat{\mathbf{e}}_2 \leftrightarrow \hat{\mathbf{e}}_1$ for a planar degeneracy or $\hat{\mathbf{e}}_2 \leftrightarrow \hat{\mathbf{e}}_3$ for a linear degeneracy. For a linear degeneracy where $\lambda_2 = \lambda_3 < 0$ and $\lambda_1 = -2\lambda_2$, the ridges in λ_2/λ_3 and the mode μ_M correspond to the valleys in λ_2/λ_1, and for a planar degeneracy where $\lambda_1 = \lambda_2 > 0$ and $\lambda_3 = -2\lambda_2$ and the ridges in λ_2/λ_1 correspond to the valleys in the mode μ_M and λ_2/λ_3. Regions on the far side of these boundaries have a pair of eigenvectors which are swapped while on the near side of these boundaries (i.e. towards the source), the eigenvectors are unchanged.

Finally, our investigation of real gradient tensor data from the Diavik diamond field reveals a pipe anomaly with a strong reversed magnetisation. These data produce consistent estimates of magnetisation direction at the observed NSS peak using the gradient tensor, its NSS and at least one of the eigenvectors. These results have been confirmed by inversion of the full gradient tensor in regions which are free of eigenvector degeneracies and which allow for the estimation of background noise levels in the gradient tensor data. This confirms that gradient tensor surveys which employ a closer line spacing are ideal for the investigation of pipe-like anomalies. Furthermore data from these surveys can be used to provide initial estimates of the bulk properties, including magnetisation intensity and magnetisation direction associated with pipe-like anomalies. We have shown that these estimates of model parameters for a vertical pipe provide an excellent starting point for inversion using gradient tensor data.

Additional research is required to recognise and quantify the effects of noise on the parameter estimates as well as any effects caused by geometric deviations from a perfect cylinder. We also need to better diagnose when NSS maxima occur between flight lines and how this affects estimates of magnetisation direction and whether this can be remedied using alternative techniques, for example, by averaging of magnetisation directions. Further work is required into understanding complexities in the NSS which relate to the inclination of magnetisation and finding a physical explanation for noted discrepancies in magnetisation directions derived from the first and third eigenvectors.

Acknowledgements

First we thank Mufaro Chivasa of Diavik Diamond Mines Inc. (DDMI) for granting us access to the Diavik gradient tensor data and giving permission to publish our research findings. Second we would like to thank David Pratt (Tensor Research) for his work in preparing the Diavik gradient tensor survey data for use in this paper. We thank Mark Lackie for his helpful suggestions in reviewing the manuscript. Also we would like to acknowledge Clive Foss, David Clark and David Pratt for their ongoing support and encouragement into research on the uses of the magnetic gradient tensors in exploration.

Disclosure statement

No potential conflict of interest was reported by the author(s).

Data availability statement

We understand that DDMI do not wish to make their magnetic gradient tensor data available for use by any external researchers, research institutions or any other outside organisation.

References

Abramowitz, M., and I.A. Stegun. 1964. *Handbook of mathematical functions, applied mathematical series*. vol. 58. New York: Dover Publications.

Anton, H., and C. Rorres. 2000. *Elementary linear algebra: Applications version*. 8th ed. Hoboken, NJ: John Wiley & Sons.

Austin, J.R., and C.A. Foss. 2014. The paradox of scale: reconciling magnetic anomalies with rock magnetic properties for cost-effective mineral exploration. *Journal of Applied Geophysics* 104: 121–133.

Austin, J., S. Geuna, D. Clark, and D. Hillan. 2014. Remanence, self-demagnetisation and their ramifications for magnetic modelling of iron oxide copper-gold deposits: An example from Candelaria, Chile. *Journal of Applied Geophysics* 109: 242–255. doi:10.1016/j.jappgeo.2014.08.002.

Beiki, M., D.A. Clark, J.R. Austin, and C.A. Foss. 2012. Estimating source location using normalised magnetic source strength estimated from gradient tensor data. *Geophysics* 77: J23–J37.

Blakely, R.J. 1995. *Potential theory in gravity and magnetic applications*. Cambridge: Cambridge University Press.

Clark, D.A. 2012. New methods for interpretation of magnetic vector and gradient tensor data I: Eigenvector analysis and the normalised source strength. *Exploration Geophysics* 43: 267–282.

Clark, D.A. 2013. New methods for interpretation of magnetic vector and gradient tensor data II: Application to the Mount Leyshon anomaly. *Exploration Geophysics* 44: 114–127. doi:10.1071/EG12066.

Clark, D.A. 2014. Methods for determining remanent and total magnetisations of magnetic sources – A review. *Exploration Geophysics* 45: 271–304.

Collinson, D. 1983. *Methods in rock magnetism and palaeomagnetism*. London: Chapman and Hall.

Cowan, E.W. 1968. *Basic electromagnetism*. Cambridge, MA: Academic Press.

Eason, G., B. Noble, and I.N. Snedden. 1955. Of certain integrals of the Lipschitz-Hankel type involving products of Bessel functions. *Philosophical Transactions of the Royal Society of London, Series A* 247: 529–551.

Foss, C. 2006. Evaluation of strategies to manage remanent magnetisation effects in magnetic field inversion. *76th Annual General Meeting SEG*, Extended Abstracts, 938–942.

Foss, C.A. 2017. Resultant-magnetisation based magnetic field interpretation. In *Proceedings of exploration 17: Sixth decennial international conference on mineral exploration*, eds. V. Tschirhart, and M.D. Thomas, 637–648.

Foss, C., and J. Austin. 2023. Distal, proximal and sweet spot limitations in source information content of magnetic field data. In *4th AEGC conference*, 13–18 March 2023, Brisbane, Australia, 6.

Foss, C., and B. McKenzie. 2011. Inversion of anomalies due to remanent magnetisation: An example from the Black Hill Norite of South Australia. *Australian Journal of Earth Sciences* 58: 391–405.

Fullagar, P.K., and G.A. Pears. 2015. Remanent magnetisation inversion: Australian society of exploration geophysicists. In *24th International geophysical conference and exhibition*, Perth, Extended Abstracts, Australia.

Graham, I., D. Burgess, D. Bryan, P.J. Ravencroft, E. Thomas, B.J. Doyle, R. Hopkins, and K.A. Armstrong. 1999. Exploration history and geology of the Diavik Kimberlites, Lac de Gras, Northwest Territories, Canada. In *Dawson volume*, Proceedings of the VIIth International conference, eds. J.J. Gurney, J.L. Gurney, M.D. Pascoe, and S.H. J.B. Richardson, 262–279. Cape Town: Red Roof Design.

Jackson, J.D. 1999. *Classical electrodynamics*. 3rd ed. Hoboken, NJ: John Wiley & Sons.

Lockhart, G., H. Grütter, and J. Carlson. 2004. Temporal, geomagnetic and related attributes of kimberlite magmatism at Ekati, Northwest Territories, Canada. *Lithos* 77: 665–682.

McKenzie, K.B. 2020. The magnetic gradient tensor of a triaxial ellipsoid, its derivation and its application to the determination of magnetisation direction. *Exploration Geophysics* 51: 609–641.

McKenzie, K.B. 2022. The magnetic field and magnetic gradient tensor for a right circular cylinder. *Exploration Geophysics* 53: 329–358.

Medeiros, W.E., and J.B.C. Silva. 1995. Simultaneous estimation of total magnetisation direction and 3-D spatial orientation. *Geophysics* 60: 1365–1377. doi:10.1190/1.1443872.

Mikhailov, M.N., G. Pajot, N. Diament, and A. Price. 2007. Tensor deconvolution: A method to locate equivalent sources from full tensor gravity data. *Geophysics* 72: I61–I69. doi:10.1190/1.2749317.

Müller, R.D., S. Zahirovic, S.E. Williams, J. Cannon, M. Seton, D.J. Bower, M.G. Tetley, et al. 2019. A global plate model including lithospheric deformation along major rifts and orogens since the Triassic. *Tectonics* 38: 1884–1907. doi:10.1029/2018TC005462.

Palacios, J., H. Yeh, W. Wang, Y. Zhang, R.S. Laramee, R. Sharma, T. Schultz, and E. Zhang. 2016. Feature surfaces in symmetric tensor fields based on eigenvalue manifold. *IEEE Transactions on Visualization and Computer Graphics* 22: 1248–1260.

Pedersen, L.B., and T.M. Rasmussen. 1990. The gradient tensor of potential field anomalies: Some implications on data collection and data processing of maps. *Geophysics* 55: 1558–1566. doi:10.1190/1.1442807.

Phillips, J.D., M.N. Nabighian, D.V. Smith, and Y. Li. 2007. Estimating locations and total magnetisation vectors of compact magnetic sources through combined Helbig and Euler analysis. *SEG Expanded Abstracts* 26: 770–774.

Pilkington, M., and M. Beiki. 2013. Mitigating remanent magnetisation effects in magnetic data using the normalised source strength. *Geophysics* 78: J25–J32. doi:10.1190/geo2012-0225.1.

Pratt, D., and K.B. McKenzie. 2009. Maximising geological information recovery from different magnetic instruments through the application of joint inversion. Australian society of exploration geophysicists. In *20th International geophysical conference and exhibition*, Adelaide, Extended Abstracts, Australia.

Pratt, D.A., K.B. McKenzie, and A.S. White. 2012. The remote determination of magnetic remanence. Australian society of exploration geophysicists. In *22nd International geophysical conference and exhibition*, February 26–29, Brisbane, Extended Abstracts, Australia, 5.

Pratt, D.A., K.B. McKenzie, and A.S. White. 2014. Remote remanence estimation (RRE). *Exploration Geophysics* 45: 314–323.

Pratt, D.A., K.B. Mckenzie, and A.S. White. 2019. An AI approach to automated magnetic formation mapping below cover. *AEGC 2019*, Perth, Australia, ASEG Extended Abstracts, 5p.

Press, W.H., S.A. Teukolsky, W.T. Vetterling, and B.P. Flannery. 1992. *Numerical recipes in Fortran the art of scientific computing*, 2nd ed. Cambridge University Press.

Qu, B., L. Roy, Y. Zhang, and E. Zhang. 2020. Mode surfaces of symmetric tensor fields: Topological analysis and seamless extraction. *IEEE Transactions on Visualisation and Computer Graphics* 27: 583–592.

Reed, L.E., and K.E. Witherly. 2007. 50 years of kimberlite geophysics, A review. In *Proceedings of exploration 07: Fifth decennial International conference on mineral exploration*, ed. B. Milkereit, 679–689.

Schmidt, P. W., and D. A. Clark. 2006. The magnetic gradient tensor: its properties and uses in source characterization. *The Leading Edge* 25: 75–78. doi:10.1190/1.2164759.

Siew, P.F. 1990. Magnetic anomalies of cylinders. *Quarterly Journal of Mechanics and Applied Mathematics* 43: 373–385.

Takahashi, D., and V.C. Oliviera. Jr. 2017. Ellipsoids (v1.0): 3-D magnetic modelling of ellipsoidal bodies. *Geoscience Model Development* 10: 3531–3608.

Taniguchi, T. 2018. An analytical computation of magnetic field generated from a cylinder ferromagnet. *Journal of Magnetism and Magnetic Materials* 452: 464–472.

Wilson, H. 1985. Analysis of the magnetic gradient tensor. *Defence Research Establishment. Pacific, Canada, Technical Memorandum* 85-13: 47.

Wynn, W.M. 1999. Detection, location and characterisation of static magnetic dipole sources. In *Detection and identification of visually obscured targets*, ed. C. E. Baum, 337–374. London: Taylor and Francis.

Wynn, W.N., C.P. Frahm, P.J. Carroll, R.H. Clark, J. Wellhoner, and M.J. Wynn. 1975. Advanced superconducting gradiometer/magnetometer arrays and a novel signal processing technique. *IEEE Transactions on Magnetics* 11: 701–707.

Appendix 1. Tensor rotational invariants, tensor attributes

The gravity gradient and magnetic gradient tensors may be calculated by forward modelling or from survey measurements or it may be computed from a grid of high resolution gravity g_z or total magnetic intensity b_T data using the wavenumber domain phase filters described in Blakely (1995).

Three eigenvalues $\lambda_1, \lambda_2, \lambda_3$ are obtained by the eigenvector decomposition of the magnetic or gravity gradient tensor (Pedersen and Rasmussen, 1990; Mikhailov *et al.*, 2007; Clark, 2012). In the magnetic case this involves finding three eigenvectors $\hat{\mathbf{e}}_1, \hat{\mathbf{e}}_2, \hat{\mathbf{e}}_3$ which satisfy the linear equation $\mathbf{B}\,\hat{\mathbf{e}}_i = \lambda_i\,\hat{\mathbf{e}}_i$ where λ_i is the eigenvalue corresponding to $\hat{\mathbf{e}}_i$. The eigenvalues are found by solving the characteristic equation $\det(\mathbf{B} - \lambda\,\mathbf{I}) = 0$. Expanding the characteristic equation results in the following cubic equation in λ:

$$\lambda^3 - I_0\lambda^2 + I_1\lambda - I_2 = 0. \tag{A1.1}$$

Or more generally,

$$\lambda^3 + \alpha_2\lambda^2 + \alpha_1\lambda + \alpha_0 = 0, \tag{A1.2}$$

where $\alpha_2 = -I_0$; $\alpha_1 = I_1$; $\alpha_0 = -I_2$.

The roots $\lambda_1, \lambda_2, \lambda_3$ of any general cubic equation satisfy the following relations (Abramowitz and Stegun, 1964, p.17, 3.8.2):

$$\begin{aligned}\lambda_1 + \lambda_2 + \lambda_3 &= I_0 = -\alpha_2\\ \lambda_1\lambda_2 + \lambda_1\lambda_3 + \lambda_2\lambda_3 &= I_1 = \alpha_1\\ \lambda_1\lambda_2\lambda_3 &= I_2 = -\alpha_0\end{aligned} \tag{A1.3}$$

However in this instance, the coefficient I_0 of the λ^2 term in equation (A1.1) is identically zero, since, at a measurement point in a source free region, the gradient tensor $\mathbf{B}$ is traceless, $B_{xx} + B_{yy} + B_{zz} = 0$. Therefore, the characteristic equation for the eigenvalues is actually a depressed cubic equation. The coefficients I_0, I_1 and I_2 in equation (A1.3) are the tensor canonical invariants of Pedersen and Rasmussen (1990). These parameters which are invariant under rotation (Clark, 2012) are related to the $\alpha_0, \alpha_1, \alpha_2$ coefficients of Abramowitz and Stegun (1964) as follows:

$$I_0 = \lambda_1 + \lambda_2 + \lambda_3 = B_{xx} + B_{yy} + B_{zz} = -\alpha_2 = 0, \tag{A1.4.1}$$

$$\begin{aligned}I_1 &= \lambda_1\lambda_2 + \lambda_1\lambda_3 + \lambda_2\lambda_3\\ &= B_{xx}B_{yy} + B_{xx}B_{zz} + B_{yy}B_{zz} - B_{xy}^2 - B_{xz}^2 - B_{yz}^2,\end{aligned} \tag{A1.4.2}$$

$$\begin{aligned}I_2 = \det\mathbf{B} &= \lambda_1\lambda_2\lambda_3 = B_{xx}B_{yy}B_{zz} - B_{xx}B_{yz}^2\\ &\quad - B_{yy}B_{xz}^2 - B_{zz}B_{xy}^2 + 2B_{xy}B_{xz}B_{yz}.\end{aligned} \tag{A1.4.3}$$

The expressions for the roots of a general cubic equation with real coefficients are well known in the literature [see Abramowitz and Stegun (1964, p.17) or Press *et al.* (1992, pp.179-180)]. In terms of the rotational invariants, the eigenvalues λ_i of the magnetic and gravity gradient tensors are as follows:

$$\lambda_1 = -2\sqrt{-\frac{I_1}{3}}\cos\left(\frac{\theta}{3}\right) \text{ or } \lambda_1 = (\mathrm{E} + \mathrm{F}), \tag{A1.5.1}$$

$$\begin{aligned}\lambda_2 &= -2\sqrt{-\frac{I_1}{3}}\cos\left(\frac{\theta}{3} + \frac{2\pi}{3}\right) \text{ or}\\ \lambda_2 &= -\frac{(\mathrm{E} + \mathrm{F})}{2} + \frac{(\mathrm{E} - \mathrm{F})}{2}i\sqrt{3},\end{aligned} \tag{A1.5.2}$$

$$\begin{aligned}\lambda_3 &= -2\sqrt{-\frac{I_1}{3}}\cos\left(\frac{\theta}{3} - \frac{2\pi}{3}\right) \text{ or}\\ \lambda_3 &= -\frac{(\mathrm{E} + \mathrm{F})}{2} - \frac{(\mathrm{E} - \mathrm{F})}{2}i\sqrt{3},\end{aligned} \tag{A1.5.3}$$

where

$$\begin{aligned}E &= \left[\frac{I_2}{2} + \left[\left(\frac{I_2}{2}\right)^3 + \left(\frac{I_1}{3}\right)^3\right]^{\frac{1}{2}}\right]^{\frac{1}{3}},\\ F &= \left[\frac{I_2}{2} - \left[\left(\frac{I_2}{2}\right)^2 + \left(\frac{I_1}{3}\right)^3\right]^{\frac{1}{2}}\right]^{\frac{1}{3}},\end{aligned} \tag{A1.6.1}$$

$$\begin{aligned}&\text{and } \theta = \arccos\left(\frac{R}{\sqrt{-Q^3}}\right);\ Q = \frac{\alpha_1}{3} = \frac{I_1}{3};\\ &R = -\frac{\alpha_2}{2} = \frac{I_2}{2},\end{aligned} \tag{A1.6.2}$$

And from equation (A1.6.2), the θ parameter is related to the dimensionless quantity I which was first introduced by Pedersen and Rasmussen (1990), namely,

$$I = \cos^2\theta = \left(\frac{R^2}{-Q^3}\right) = -\left(\frac{I_2}{2}\right)^2 \Big/ \left(\frac{I_1}{3}\right)^3 = -\frac{27I_2^2}{4I_1^3}. \tag{A1.7}$$

This necessarily implies that the I_1 tensor invariant must be negative otherwise θ is physically unrealisable. Furthermore a necessary condition for the existence of three real eigenvalues is that

$$Q^3 + R^2 = \left(\frac{I_1}{3}\right)^3 + \left(\frac{I_2}{2}\right)^2 \le 0. \tag{A1.8}$$

When the invariant ratio $I = 1$, then $\theta = 0$ or $\theta = \pi$ and $Q^3 + R^2 = \left(\frac{I_1}{3}\right)^3 + \left(\frac{I_2}{2}\right)^2 = 0$, and there are three real eigenvalues of which two are equal, while for $I < 1$ and $Q^3 + R^2 < 0$ and $\left(\frac{I_1}{3}\right)^3 + \left(\frac{I_2}{2}\right)^2 < 0$, there are three unequal eigenvalues. This symmetry of the magnetic gradient tensor necessarily implies that the eigenvalues will always be real (see Anton and Rorres, 2010 and Clark, 2012). This means that the case in which one eigenvalue is real and the other two form a complex conjugate pair, i.e. when, $Q^3 + R^2 > 0$, never arises. We note that the expression for the Q parameter in equation A1.6.2 follows the definition given in Abramowitz and Stegun (1964) which is opposite in sign to the definition in Press et al. (1992).

Appendix 2. Analytical Basis of the Field Component Ratio Method

The expressions for the Cartesian components of the magnetic field vector $b(\mathbf{r})$ at an observation point $\mathbf{r} = (0{,}0{,}z)^T$ on the axis of a right circular vertical cylinder of radius a, axial length h and magnetisation $\mathbf{M} = (M_x, M_y, M_z)^T$ may be derived from expressions given in McKenzie (2022, equations (22.1)-(22.3) and Table 1), namely:

$$b_x(0{,}0{,}z) = \pi\, \mathrm{C_m}\, M_x \left\{ \frac{|z|}{\sqrt{a^2 + z^2}} - \frac{(|z| + h)}{\sqrt{a^2 + (|z| + h)^2}} \right\}, \tag{A2.1.1}$$

$$b_y(0{,}0{,}z) = \pi\, \mathrm{C_m} M_y \left\{ \frac{|z|}{\sqrt{a^2 + z^2}} - \frac{(|z| + h)}{\sqrt{a^2 + (|z| + h)^2}} \right\}. \tag{A2.1.2}$$

$$b_z(0{,}0{,}z) = -2\pi\, \mathrm{C_m}\, M_z \left\{ \frac{|z|}{\sqrt{a^2 + z^2}} - \frac{(|z| + h)}{\sqrt{a^2 + (|z| + h)^2}} \right\}. \tag{A2.1.3}$$

where $\mathrm{C_m} = 100$ nH/m or 100 nTm/A for magnetic fields expressed in nanotesla (nT) and magnetisations expressed in ampere per metre (A/m).

By inspection of equations (A2.1.1) and (A2.1.2), an expression for the declination of magnetisation D_M of a right circular vertical cylinder at any point $\mathbf{r} = (0,\, 0,\, z)^T$ on its axis is obtained from the signed ratio of the horizontal field components, namely,

$$D_M = \arctan\left(\frac{M_y}{M_x}\right) = \arctan\left(\frac{-b_y}{-b_x}\right) \quad \text{for } 0 \le D_M \le 2\pi. \tag{A2.2}$$

Similarly, by inspection of equations (A2.1.1)-(A2.1.3), the inclination of magnetisation I_M is obtained from the ratio of the horizontal field component to half the vertical field component, namely,

$$I_M = \arctan\left(\frac{M_z}{M_h}\right) = \arctan\left(\frac{b_z}{2\sqrt{b_x^2 + b_y^2}}\right) \quad \text{for} \quad -\frac{\pi}{2} \le I_M \le \frac{\pi}{2}. \tag{A2.3}$$

The magnetic gradient tensor $\mathbf{B}(0{,}0{,}z)$ on the axis of a uniformly magnetised right circular vertical pipe with radius a and axial length h is

$$\mathbf{B}(0,\, 0,\, z) = \begin{bmatrix} B_{xx} & B_{xy} & B_{xz} \\ B_{yx} & B_{yy} & B_{yz} \\ B_{zx} & B_{zy} & B_{zz} \end{bmatrix} = \beta \begin{bmatrix} -M_z & 0 & -M_x \\ 0 & -M_z & -M_y \\ -M_x & -M_y & 2M_z \end{bmatrix}, \tag{A2.4}$$

where $\beta = \pi\, a^2\, \mathrm{C_m} \left\{ \frac{1}{(a^2+z^2)^{3/2}} - \frac{1}{(a^2+(|z|+h)^2)^{3/2}} \right\}$.

By inspection of equations (A2.2) and (A2.4), the declination of magnetisation D_M at any point on the axis of a right circular vertical cylinder is obtained from the ratio of the B_{xz} and B_{yz} tensor elements as follows:

$$D_M = \arctan\left(\frac{M_y}{M_x}\right) = \arctan\left(\frac{-B_{yz}}{-B_{xz}}\right) \quad \text{for } 0 \le D_M \le 2\pi. \tag{A2.5}$$

Similarly, by inspection of equations (A2.3) and (A2.4), the inclination of magnetisation I_M at any point on the axis of a right circular vertical cylinder is derived from the B_{xz} , B_{yz} and B_{zz} tensor elements as follows:

$$I_M = \arctan\left(\frac{M_z}{M_h}\right) = \arctan\left(\frac{B_{zz}}{2\sqrt{B_{xz}^2 + B_{yz}^2}}\right) \quad \text{for} \quad -\frac{\pi}{2} \le I_M \le \frac{\pi}{2}. \tag{A2.6}$$

Appendix 3. NSS anomaly half-width: The effect of magnetisation direction and observation height

The NSS of a long or compact vertical pipe peaks over its centre for all observation heights $|z|/a \ge 1$. This facilitates direct comparisons between the half-widths of the NSS along different directions parallel, antiparallel, and perpendicular to the declination of magnetisation. This paper has already demonstrated asymmetry in the NSS of a vertical cylinder which is not present for point pole or dipole sources and that this asymmetry is entirely due to the horizontal component of magnetisation. The effect on NSS half-widths is now investigated for a range of standardised observation heights and inclinations of magnetisation I_M from -90° to 0°.

Figures A3.1a and A3.1b show the variation in half-width of the NSS parameter for principal profiles parallel and perpendicular to D_M for a series of semi-infinite vertical pipes with variable inclination of magnetisation, i.e. $I_M =$ -90°, -75°, -60°, -45°, -30° and 0°, in which the standardised observation height $|z|/a$ ranges from 1 to 10. Figure A3.2 shows the change in NSS half-width ratio $x_{\mathrm{hw}\mu}/|z|$ both parallel and anti-parallel to D_M as the inclination of magnetisation I_M is varied from -90° to 0° for three standardised observation heights $|z|/a = 2, 4, 10$.

The NSS half width plots in Figures A3.1a and A3.1b decline rapidly towards 1 as $|z|/a$ increases from 1 to 2. The effect of inclination of magnetisation on the NSS half-widths is not significant for $|z|/a < 1.5$, but for observation heights $|z|/a > 2$, the NSS half-widths asymptote towards different limits depending upon the inclination of magnetisation and the direction of the principal profile (in relation to D_M) as the observation height becomes very large (i.e. $|z|/a \ge 10$). The magnetic point pole is directly analogous to a narrow, vertically magnetised semi-infinite circular pipe. Clark (2012) gives an expression for the NSS of a magnetic point pole with vertical magnetisation M_z and cross-sectional area A:

$$\mu_{\mathrm{pole}}(r) = \frac{\mathrm{C_m} M_z A}{r^3} = \frac{\mathrm{C_m} M_z A}{(x^2 + z^2)^3}. \tag{A3.1}$$

Hence it may be shown that the NSS half-width $x_{\mathrm{hw}\mu}^{\mathrm{pole}}$ for a point pole is

$$x_{\mathrm{hw}\mu}^{\mathrm{pole}} = \left(\sqrt[3]{4} - 1\right)^{1/2} |z| \quad \text{or} \quad x_{\mathrm{hw}\mu}^{\mathrm{pole}} \cong 0.76642|z|. \tag{A3.2}$$

From equation 2 and for purposes of comparison, the NSS half-width $x_{\mathrm{hw}\mu}^{\mathrm{dp}}$ for a dipole is

$$x_{\mathrm{hw}\mu}^{\mathrm{dp}} = \left(\sqrt{2} - 1\right)^{1/2} |z| \quad \text{or} \quad x_{\mathrm{hw}\mu}^{\mathrm{dp}} \cong 0.64359|z|. \tag{A3.3}$$

Figures A3.1a, A3.1b and A3.2 show that the half-widths for a right circular vertical pipe with a vertical magnetisation $I_M =$

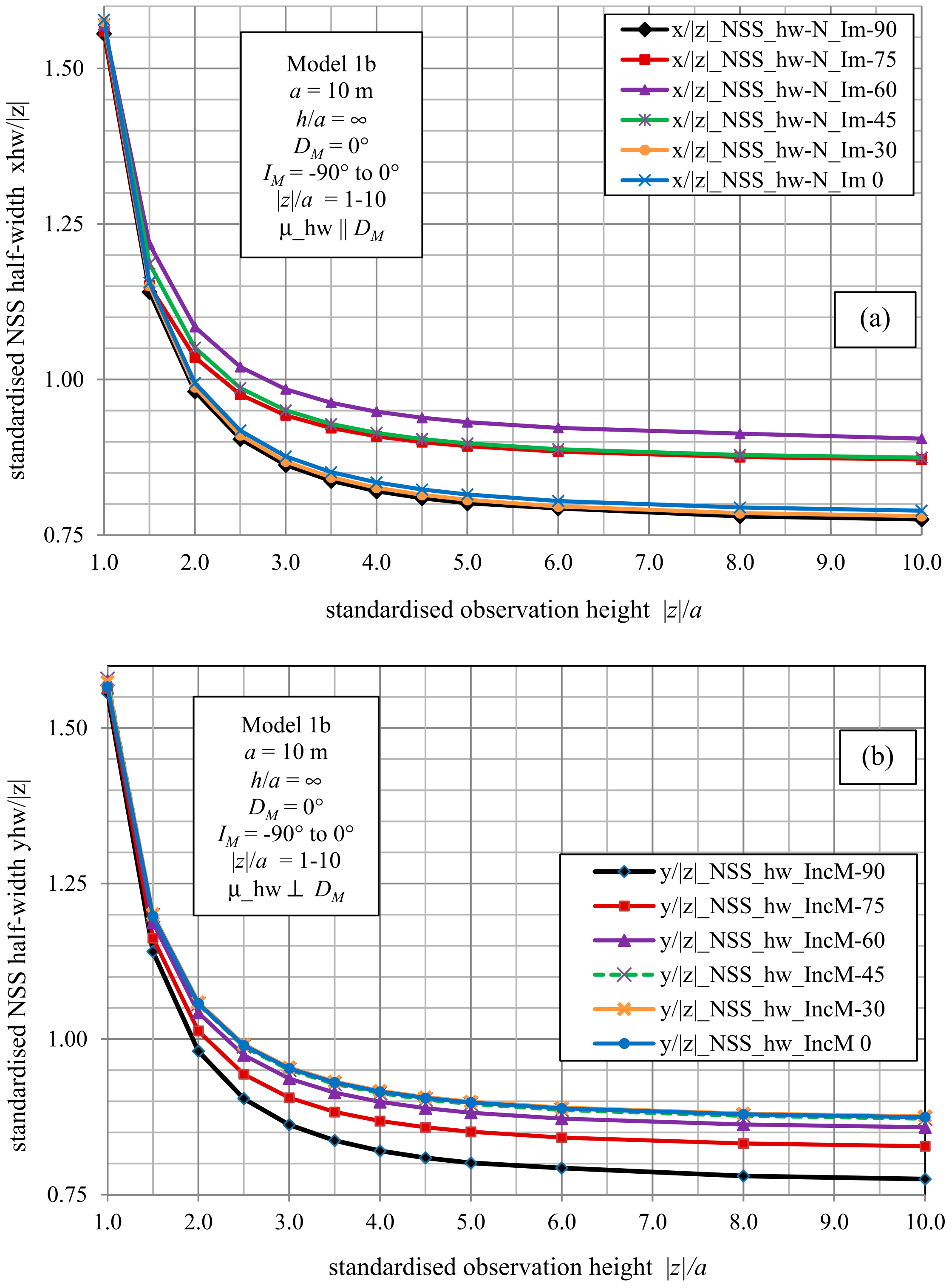

Figure A3.1. Plots showing the variation in half-width ratio $x_{hw\mu}/|z|$ of the NSS parameter with increasing standardised observation height. Figures A3.1a and A3.1b show the half-width ratios for principal profiles parallel and perpendicular to D_M respectively for a series of semi-infinite, right circular, vertical pipes with variable inclination of magnetisation, i.e. I_M = -90°, -75°, -60°, -45°, -30° and 0°. The standardised observation height $|z|/a$ ranges from 1 to 10.

-90° all asymptote towards the theoretical limit for a point pole as $|z|/a$ approaches 10. For principal profiles perpendicular to D_M in Figure A3.1b, the half-width ratios $x_{hw\mu}/|z|$ all appear to asymptote towards a higher limit with the half-width ratios for mid-range to low inclination angles (-45° $\leq I_M \leq$ 0°) all in the range from 0.872-0.876 at $|z|/a = 10$. The half-width ratios $x_{hw\mu}/|z|$ at low to high inclinations for profiles antiparallel to D_M are closely clustered and asymptote towards a limit slightly below 0.80 (see Figure A3.2). In contrast, the half-width ratios $x_{hw\mu}/|z|$ at mid to high inclinations for profiles parallel to D_M all appear to converge towards higher limits, namely, at $|z|/a = 10$, $x_{hw\mu}/|z| = 0.905$ for I_M = -60° and $x_{hw\mu}/|z| = 0.875$ for I_M = -45° (see Figures A3.1a and A3.2). Interestingly, the NSS half-width ratios parallel to D_M in Figure A3.2 display peaks for I_M = -60° at all observation heights $|z|/a \geq 1$. These maxima in the half-width ratios at I_M = -60° correspond to maxima in

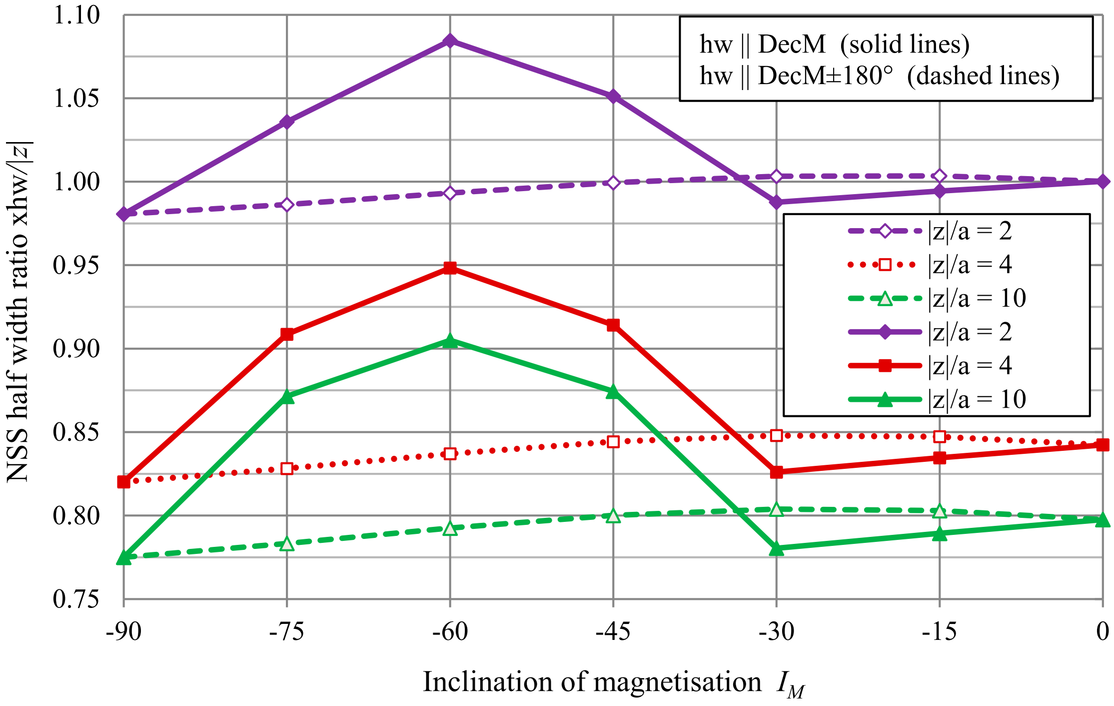

Figure A3.2. Plots showing the change in NSS half-width ratio $x_{hw\mu}/|z|$ both parallel and antiparallel to D_M as the inclination of magnetisation I_M changes from -90° to 0° for three standardised observation heights $|z|/a = 2, 4, 10$.

the NSS $\mu_{pmax}^{h/a=\infty}$ which extend into the proximal region of the NSS at $|z|/a \leq 0.5$ as shown in Figure 4. Curiously, the results at low inclinations I_M = -30° to I_M = 0° are much closer to the theoretical limit of 0.766 for a vertical magnetisation or magnetic pole (see Figure A3.1a and Figure A3.2). This is also confirmed at low observation heights $|z|/a \leq 0.5$ in Figure 4 where the NSS maxima are significantly lower in the vicinity of I_M = -30°. There is a complexity in these results that is not easily explained from a physical standpoint and which requires further investigation.

Appendix 4. The effect of axial length on the NSS at low sensor observation heights

This appendix investigates the effect of increasing axial length on the NSS μ as the standardised axial length h/a of a vertical cylinder is varied from 0.1 to 10. This study applies to gradient tensor data flown at relatively low observation heights (0.5 $\leq |z|/a \leq 2$) over near surface pipes. This information can be important in planning gradient tensor surveys. Not only can the NSS be used to determine the horizontal centre of magnetisation, but it may also be used to estimate the effective vertical centre of magnetisation (eVCM) for a vertical pipe as its axial length h/a increases. We define the eVCM for gradient tensor data as the axial length h_{evcm} which yields 50 % of the observed NSS maximum for a vertical cylinder of axial length h. The true VCM of a vertical cylinder is at half its axial length.

The effect of increasing standardised axial length h/a on the normalised NSS maxima is shown in Figure A4.1 for a series of vertical pipes with h/a = 0.1, 0.2, 0.3, 1, 2, 3, 5, 10 at a low standardised height $|z|/a = 0.5$. Plots of the normalised NSS maxima for principal profiles parallel $\mu_{pmax}^{h/a}$ and antiparallel $\mu_{apmax}^{h/a}$ to D_M are shown in red and blue respectively. The normalised NSS data on the axis of the circular pipe D_M $\mu_{axis}^{h/a}$ are shown in black. All global maxima have been normalised by the maximum value $\mu_{pmax}^{h/a=\infty}$ for a semi-infinite vertical pipe. The $\mu_{axis}^{h/a}$ data on the axis of the circular pipe are consistently lower than $\mu_{pmax}^{h/a}$ and $\mu_{apmax}^{h/a}$ at each axial length h/a. The plots in Figure A4.1 illustrate the strong asymmetry in the NSS for directions parallel, antiparallel and perpendicular to D_M at low observation heights.

For a long vertical pipe with $h/a = 10$, the effective vertical centre of magnetisation for $\mu_{pmax}^{h/a=10}$ and $\mu_{apmax}^{h/a=10}$ is reached at a standardised axial length $h/a = 0.3$ (i.e. as for a circular disc) which represents only the top 3 % of the total length of the pipe. For an equidimensional compact cylinder where h/a = 2, $\mu_{pmax}^{h/a=2}$ exceeds 92.8 % of the global maximum $\mu_{pmax}^{h/a=\infty}$, and at $h/a = 5$, $\mu_{pmax}^{h/a=5}$ exceeds 99.2 % of $\mu_{pmax}^{h/a=\infty}$. Hence at a low standardised observation height $|z|/a = 0.5$, almost the entire observed maximum NSS signal originates from near the top of a right circular vertical pipe, and therefore, it is extremely difficult to determine the true depth extent of a long vertical pipe. From Figure A4.1, the effective vertical centres of magnetisation (effective VCM) for a series of vertical pipes with h/a = 0.5, 1, 2, 5 are at ~0.164a, ~0.233a, ~0.280a, ~0.292a respectively, which represents 32.8 %, 23.3 %, 14.0 % and 5.84 % of the total length for each pipe.

Since the NSS peaks on the axis of a vertical cylinder, the effect of axial length on the NSS at standardised observation heights $|z|/a \geq 1.0$ may be determined from equation (8), namely, $\mu_{max}^{h/a} = \beta_h|\mathbf{M}|$. Hence for $|z|/a \geq 1$, the ratio of the NSS maxima $\mu_{max}^{h}/\mu_{max}^{\infty}$ for a pair of cylinders of radius a, magnetisation M and axial lengths h and ∞ is

$$\mu_{max}^{h}/\mu_{max}^{\infty} = \beta_h/\beta_\infty = \left\{1 - \left[\frac{1+(|z|/a)^2}{1+(|z|/a+h/a)^2}\right]^{3/2}\right\}, \quad \text{(A4.1)}$$

where $\beta_h = \frac{\pi C_m}{a}\left\{\frac{1}{[1+(|z|/a)^2]^{3/2}} - \frac{1}{[1+(|z|/a+h/a)^2]^{3/2}}\right\}$.

Table A4.1 shows the relative contributions to the axial NSS ratio from the uppermost 10 %, 20 %, and 50 % of a long vertical pipe with axial length $h/a = 5$. These results confirm that for observation heights $|z|/a$ between 1 and 2, nearly all

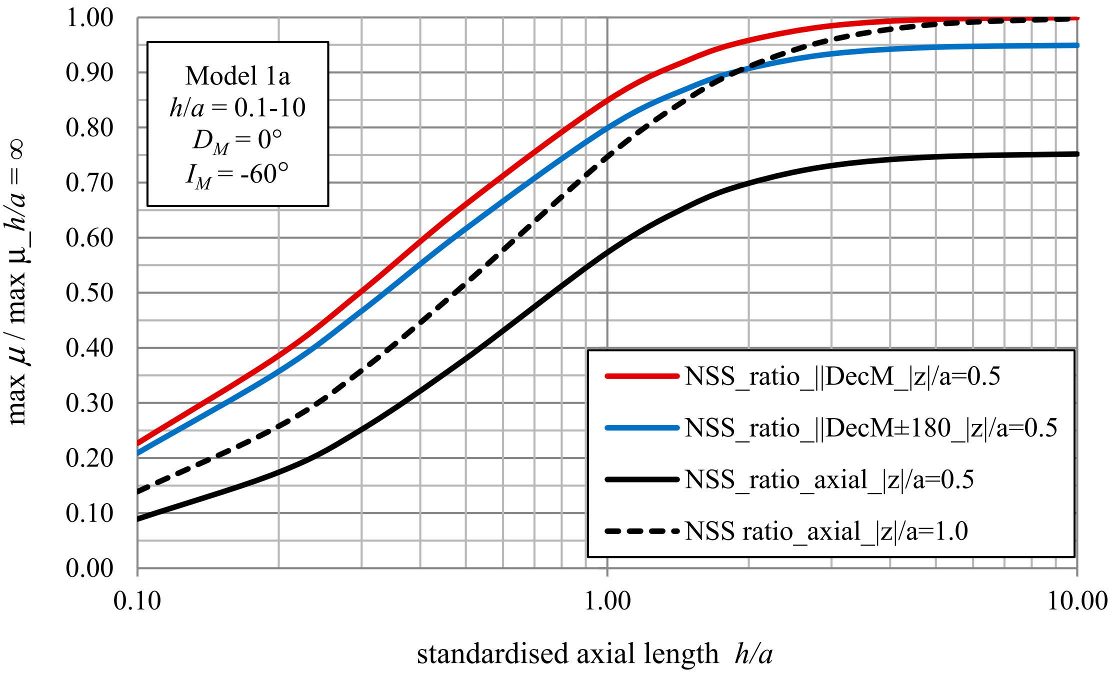

Figure A4.1. Log-linear plots which show the relative variation in the maximum NSS ratios parallel $\mu^{h/a}_{\text{pmax}}/\mu^{h/a=\infty}_{\text{pmax}}$, antiparallel $\mu^{h/a}_{\text{apmax}}/\mu^{h/a=\infty}_{\text{pmax}}$ and axial $\mu^{h/a}_{\text{axial}}/\mu^{h/a=\infty}_{\text{pmax}}$ with standardised axial length (h/a) for a series of finite length, right circular, vertical pipes with a high inclination of magnetisation $I_M = -60°$. The standardised observation height for the two axial cases are $|z|/a = 0.5$ and 1.0.

Table A4.1. Relative contribution to the maximum NSS of a right circular vertical cylinder with standardised axial length $h/a = 5$ for a series of observation heights $|z|/a = 1.0, 1.25, 1.5$, and 2.0.

NSS contribution	h/a	$z/a = 1.00$	$z/a = 1.25$	$z/a = 1.50$	$z/a = 2.00$
upper 10 %	0.5	51.11	49.08	46.49	40.86
upper 20 %	1.0	74.38	72.07	69.36	63.49
upper 50 %	2.5	94.06	92.87	91.47	88.21

the maximum NSS signal (exceeding 94 % for $|z|/a = 1$) for a long vertical cylinder originates from its uppermost 50 % . These contributions decrease slightly with increasing observation height and in more compact cylinders (i.e. for $h/a = 2$). We also note that the effective VCM for $|z|/a = 1.25$ (cf. with Diavik anomaly A in Table 3) is at $h/a = 0.490$ below the top surface which represents the uppermost 9.80 % of the vertical cylinder with $h/a = 5$.

Appendix 5. Supplementary NSS data for the right circular vertical cylinder and its equivalent magnetic sphere

From Table A5.1, it is noted that the ratio $z_s/|z|$ decreases with increasing standardised observation height $|z|/a$ in each of the vertical pipes. Furthermore the depth z_s decreases towards $|z|$ as the axial length h/a increases from 4/3 to infinity

Table A5.1. Depth ratios $z_s/|z|$ (computed from equation (26)) for a series of equivalent magnetic spheres which possess the same NSS as a series of finite length and semi-infinite right circular vertical cylinders with axial lengths ranging from $h/a = 4/3, 2, \ldots, 10$ and ∞. The standardised observation heights for the vertical cylinder range from $|z|/a = 1$ to $|z|/a = 10$. Both the pipe models and their equivalent magnetic spheres have the same radius a and magnetisation **M.**

$\|z\|/a$	$z_s/\|z\|$ $h/a = 4/3$	$z_s/\|z\|$ $h/a = 2.0$	$z_s/\|z\|$ $h/a = 3.0$	$z_s/\|z\|$ $h/a = 5.0$	$z_s/\|z\|$ $h/a = 10.0$	$z_s/\|z\|$ $h/a = \infty$
0.5	3.2061	3.1329	3.0980	3.0815	3.0762	3.0753
1.0	1.9231	1.8775	1.8530	1.8398	1.8350	1.8340
2.0	1.3966	1.3504	1.3218	1.3034	1.2951	1.2930
3.0	1.2496	1.1967	1.1610	1.1354	1.1219	1.1179
4.0	1.1819	1.1230	1.0811	1.0487	1.0296	1.0230
6.0	1.1178	1.0504	0.9992	0.9556	0.9258	0.9129
8.0	1.0871	1.0142	0.9566	0.9048	0.8658	0.8458
10.0	1.0691	0.9924	0.9303	0.8723	0.8257	0.7982

Table A5.2. The standardised radial distances $d_{||}/a$ and $d_{\perp}/a$ parallel and perpendicular to the magnetisation direction measured from the axis of a vertical cylinder of radius *a* to points where the NSS ratio $\alpha = \mu_s/\mu_c$ is 95 %. The first sub-table shows $d_{||}/a$; the second sub-table shows $d_{\perp}/a$ and the third sub-table shows the ratios $d_{||}/d_{\perp}$ for a series of axial lengths $h/a = 4/3$, 2.0, ∞ and observation heights $|z|/a = 1, 2, 3, 4$. The inclination of magnetisation for the pipe model is $I_M = -45°$.

h/a	$d_{\vert\vert}/a$ $\vert z\vert/a = 1$	$d_{\vert\vert}/a$ $\vert z\vert/a = 2$	$d_{\vert\vert}/a$ $\vert z\vert/a = 3$	$d_{\vert\vert}/a$ $\vert z\vert/a = 4$
4/3	0.3125	0.9375	3.2250[1]	4.2750[2]
2	0.3125	0.7750	1.3288	1.7875
∞	0.3125	0.6875	0.9625	1.1250
h/a	$d_{\perp}/a$ $\vert z\vert/a = 1$	$d_{\perp}/a$ $\vert z\vert/a = 2$	$d_{\perp}/a$ $\vert z\vert/a = 3$	$d_{\perp}/a$ $\vert z\vert/a = 4$
4/3	0.4500	1.3476	3.5250[1]	4.6000[2]
2	0.4199	0.9119	1.3899	1.8017
∞	0.3915	0.6759	0.8523	0.9846
h/a	$d_{\vert\vert}/d_{\perp}$ $\vert z\vert/a = 1$	$d_{\vert\vert}/d_{\perp}$ $\vert z\vert/a = 2$	$d_{\vert\vert}/d_{\perp}$ $\vert z\vert/a = 3$	$d_{\vert\vert}/d_{\perp}$ $\vert z\vert/a = 4$
4/3	0.694	0.696	0.915	0.929
2	0.744	0.850	0.956	0.992
∞	0.798	1.017	1.129	1.143

Note[1,2]: The $\alpha = 95\%$ radial distances $d_{||}/a$ and $d_{\perp}/a$ do not exist for $h/a = 4/3$ and $|z|/a = 3, 4$. Instead $d_{||}/a$ and $d_{\perp}/a$ are shown at the distances where the NSS ratios $\alpha = \mu_s/\mu_c$ display a minimum over the $d/a = \pm 10.00$ m search range. The NSS ratios for $d_{||}/a$ and $d_{\perp}/a$ at $|z|/a = 3$ are $\alpha = 95.20$ % and 96.61 % respectively, and for $|z|/a = 4$, $\alpha = 97.27\%$ and 98.076 %.

for all observation heights $|z|/a \leq 4$. At greater observation heights $|z|/a \geq 6$ and for more elongated pipes $h/a \geq 3$, the depth to the top surface of the pipe $|z|$ now exceeds the depth z_s to the centre of the equivalent sphere so that $z_s/|z| < 1$.

Table A5.2 displays the standardised radial distances $d_{||}/a$ and $d_{\perp}/a$ parallel and perpendicular to the magnetisation direction at points where the NSS ratios $\alpha = \mu_s/\mu_p$ are 95%. The radial distances $d_{||}/a$ and $d_{\perp}/a$ and their ratios $d_{||}/d_{\perp}$ increase with increasing observation height and also with decreasing axial length. This is particularly noticeable in Figure 8 for cylinders with $h/a = 4/3$ where the NSS ratio remains above 95% over the entire $x/a = \pm 5$ or $y/a = \pm 5$ search ranges both parallel and perpendicular to the direction of magnetisation. For the pair of compact pipes, $d_{||}/a$ is significantly below $d_{\perp}/a$ at observation heights $|z|/a \leq 2$, while for the semi-infinite pipe, this is only apparent for observation heights $|z|/a \leq 1$. Furthermore, for the semi-infinite pipe, the $d_{||}/d_{\perp}$ ratio exceeds 1 for all $|z|/a \geq 2$. In contrast, the $d_{||}/d_{\perp}$ ratios in the pair of compact pipes $h/a = 4/3, 2$ are below 75% at $|z|/a = 1$, and then increase towards 1 as $|z|/a$ approaches 4.

This observed directional asymmetry in the $d_{||}/d_{\perp}$ ratios is consistent with the azimuthal asymmetry of the NSS over right circular vertical pipes which possess a horizontal component of magnetisation. This asymmetry lessens with increasing observation height as the dipole component of magnetisation becomes dominant.